Monthly Notices of the ROYAL ASTRONOMICAL SOCIETY

MNRAS **541,** 429–445 (2025) https://doi.org/10.1093/mnras/staf938
Advance Access publication 2025 June 30

The optical, UV-plateau, and X-ray tidal disruption event luminosity functions reproduced from first principles

Andrew Mummery[1]★ and Sjoert van Velzen[2]

[1]*Oxford Theoretical Physics, Beecroft Building, Clarendon Laboratory, Parks Road, Oxford OX1 3PU, UK*
[2]*Leiden Observatory, Leiden University, Postbus 9513, NL-2300 RA Leiden, the Netherlands*

Accepted 2025 May 28. Received 2025 May 27; in original form 2024 October 22

ABSTRACT

We reproduce the luminosity functions of the early-time peak optical, the late-time ultraviolet (UV)-plateau, and the peak X-ray luminosities of tidal disruption events, using an entirely first-principles theoretical approach. We do this by first fitting three free parameters of the tidal disruption event black hole mass distribution using the observed distribution of late-time UV-plateau luminosities, using a time-dependent relativistic accretion model. Using this black hole mass distribution we are then, with no further free parameters of the theory, able to reproduce exactly the peak X-ray luminosity distribution of the tidal disruption event population. This proves that the X-ray luminosity of tidal disruption events are sourced from the same accretion flows which produce the late-time UV plateau. Using an empirical scaling relationship between peak optical luminosities and black hole masses, itself calibrated using the same relativistic accretion theory, we are able to reproduce the observed peak optical luminosity function, again with no additional free parameters. Implications of these results include that there is no tidal disruption event 'missing energy problem', that the optical- and X-ray-selected tidal disruption event populations are drawn from the same black hole mass distribution, that the early-time optical luminosity in tidal disruption events is somewhat simple, at least on the population level, and that future Legacy Survey of Space and Time (LSST) observations will be able to constrain the black hole mass function at low masses.

Key words: accretion, accretion discs – black hole physics – transients: tidal disruption events.

1 INTRODUCTION

Tidal disruption events (TDEs) occur in the centres of (previously) quiescent galaxies when an unfortunate star is scattered by N-body gravitational interactions onto a near-radial orbit about the central supermassive black hole. Once the tidal force of the black hole's space–time overcomes the star's self-gravity, the star is unbounded and becomes a debris stream which ultimately rains down onto the black hole powering bright flares observed across the electromagnetic spectrum.

A 'canonical' TDE is typically discovered as a bright flare in optical bands, which may or may not be associated with a rapid rise in X-ray flux, from the centre of a galaxy. Typical optical luminosities peak at around $L \sim 10^{43-44}$ erg s^{-1}, as do the brightest X-ray flares, before decaying away on $\sim$ month time-scales. On significantly longer time-scale ($\sim$ years) a pronounced plateau is observed in the optical/ultraviolet (UV) light curves (van Velzen et al. 2019b; Mummery & Balbus 2020) which is most easily observed in the UV (van Velzen et al. 2019b) but can also be detected in the optical (Mummery et al. 2024b). This plateau is associated with a transition from the (currently poorly understood) physics of the early-time optical flare to a disc-dominated state (Mummery & Balbus 2020; Mummery et al. 2024b).

While a rare event in any one galaxy (typical rates are of order $\sim 10^{-4}$ galaxy^{-1} yr^{-1}, Rees 1988; Magorrian & Tremaine 1999), all sky surveys in the optical (e.g. the All-Sky Automated Survey for Supernovae; Holoien et al. 2016, and Zwicky Transient Facility, van Velzen et al. 2019a; Yao et al. 2023 surveys) and X-ray (such as the X-ray Multi-Mirror Mission slew, Esquej et al. 2008, and eROSITA, Sazonov et al. 2021; Grotova et al. 2025 surveys), have lead to a growing number of known systems, a population which now stands at roughly 100 individual sources. These hard-won data sets mean that it now possible to pose questions regarding the properties of the populations of these exotic objects. This is an important step change in TDE science; while the properties of some individual sources are well described by black hole accretion models (e.g. the well-behaved source ASASSN-14li, Mummery & Balbus 2020; Wen et al. 2020), other individual sources show more extreme properties (such as large-amplitude short-time-scale variability; e.g. Wevers et al. 2021). It is an important test of theoretical models of TDEs that the gross population-level properties of these systems can be reproduced with physically reasonable parameters.

Recently, Mummery et al. (2024b) demonstrated that the late-time UV-plateau luminosity observed from TDEs offer a particularly promising route to understanding the properties of the population of TDEs. The reason for this is that the amplitude of the late-time UV luminosity is strongly correlated with the black hole mass at the centre of the event $L_{\rm plat} \propto M_\bullet^{2/3}$, meaning that the distribution of plateau luminosities observed in these systems might offer a

★ E-mail: andrew.mummery@physics.ox.ac.uk

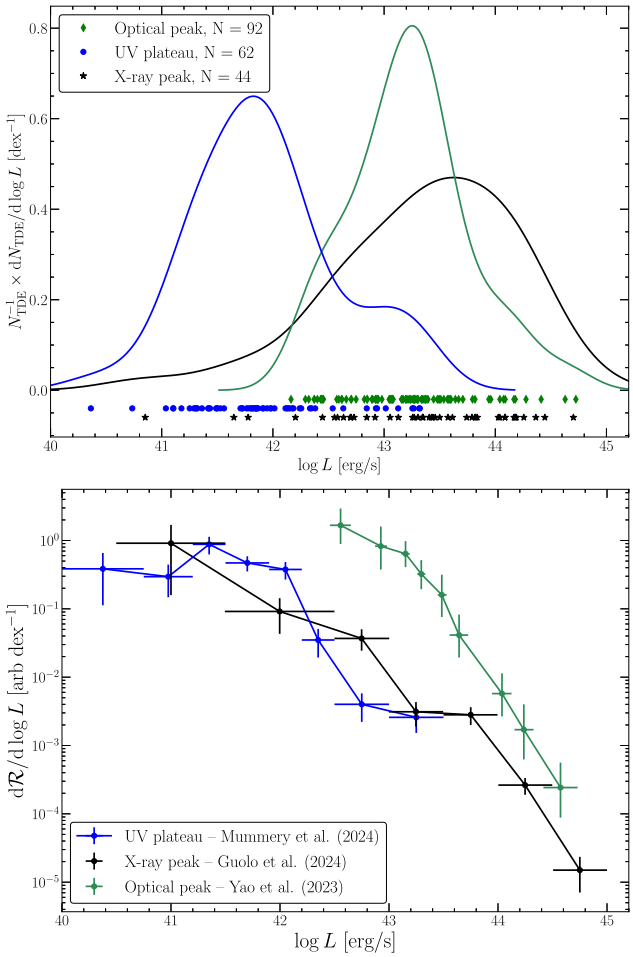

Figure 1. The observational data which we seek to reproduce in this work. Upper: the observed TDE luminosity distributions in optical (early time), UV (late time), and X-ray (peak) bands. The smooth curves are computed using Gaussian Kernel density estimation, while individual data points are shown below each curve. The structure of each luminosity distribution shows unique features. Lower: the three corresponding luminosity functions (normalized so that each curve integrates to unity). The different structures of each luminosity distribution are most noticeable when expressed in terms of intrinsic rates.

route into constraining the black hole mass distribution of these events. This represents a key step in constraining the wider (e.g. peak optical and X-ray luminosity) observed distributions of these systems. Mummery et al. (2024b) demonstrated that the masses inferred from the late-time plateau are consistent with the known $M_\bullet - \sigma$ (and $M_\bullet - M_{\rm gal}$) relationship extrapolated down from higher mass galaxies, which is a good start.

Concurrently, a number of observational surveys have lead to tight constraints being placed on the intrinsic rate at which the early-time optical (Yao et al. 2023), late-time UV (Mummery et al. 2024b), and X-ray (Guolo et al. 2024) luminosities of TDEs are distributed.[1] Current observational data constrains both the observed distributions [Fig. 1; data from Yao et al. (2023), Mummery et al. (2024b), and Guolo et al. (2024)], but also the relative rates of certain properties

[1]In this paper, we use the symbol L_g ($L_{\rm UV}$) to represent νL_ν for narrow-band observations in the g-band (UV bands), and L_X for the integrated luminosity across the broader $0.3 - 10$ keV X-ray bandpass.

Table 1. The black hole masses of the 14 new TDEs in our sample, computed from Mummery et al. (2024b) plateau luminosity scaling relationship. The quoted error ranges correspond to 1σ uncertainties. The plateau luminosity here is measured at $\nu = 10^{15}$ Hz.

TDE name	$\log_{10} L_{\rm plat}$ $\log_{10}{\rm erg\,s^{-1}}$	$\log_{10} M_\bullet$ $\log_{10}{\rm M_\odot}$
AT2017eqx	$41.98^{+0.20}_{-0.12}$	$6.81^{+0.52}_{-0.40}$
AT2018bsi	$41.83^{+0.13}_{-0.13}$	$6.62^{+0.53}_{-0.42}$
AT2019eve	$41.42^{+0.04}_{-0.06}$	$6.04^{+0.58}_{-0.45}$
AT2020ksf	$41.91^{+0.05}_{-0.05}$	$6.71^{+0.54}_{-0.42}$
AT2020vdq	$41.04^{+0.07}_{-0.07}$	$5.52^{+0.59}_{-0.46}$
AT2021ack	$41.85^{+0.11}_{-0.09}$	$6.64^{+0.54}_{-0.43}$
AT2021gje	$43.13^{+0.04}_{-0.03}$	$7.95^{+0.34}_{-0.36}$
AT2021lo	$42.84^{+0.05}_{-0.04}$	$7.74^{+0.33}_{-0.41}$
AT2022dbl	$41.18^{+0.04}_{-0.03}$	$5.68^{+0.60}_{-0.44}$
AT2022bdw	$41.53^{+0.06}_{-0.05}$	$6.19^{+0.58}_{-0.44}$
AT2022rz	$41.98^{+0.11}_{-0.10}$	$6.81^{+0.52}_{-0.41}$
AT2022hvp	$42.54^{+0.04}_{-0.04}$	$7.47^{+0.33}_{-0.38}$
AT2022dsb	$41.82^{+0.02}_{-0.02}$	$6.58^{+0.54}_{-0.40}$
AT2023clx	$40.36^{+0.12}_{-0.11}$	$4.63^{+0.65}_{-0.40}$

in the wider universe (i.e. the above distributions once Malmquist biases are corrected for; lower panel of Fig. 1).

The simplest theoretical question that can be asked is whether any one model can reproduce, from first principles, the observations summarized in Fig. 1. This question has clear physical content: the distributions and rates have fundamentally different structures (particularly when plotted as intrinsic rates) from observational band to observational band. This rules out naive models which (for example) scale each luminosity with the Eddington limit of the host black hole, as this would imply a simple shifting of the same distribution. As far as the authors are aware this question has not yet been posed in the literature. It is the purpose of this paper to demonstrate that all three distributions can be reproduced entirely with results derived from time-dependent relativistic accretion theory.

The layout of this paper is as follows. In Section 2, we introduce the TDE sample used in this work, which includes an extended UV-plateau population. In Section 3, we introduce the underlying theoretical framework used in this paper, and review the accretion models introduced in Mummery et al. (2024b). In Section 4, we present the results of our analysis, before discussing their implications in Section 5. We conclude in Section 6. A detailed description of the statistical formalism used in constraining the parameters of the black hole mass distribution is presented in Appendix A.

2 THE OBSERVED TDE POPULATION

In this work, we use the `manyTDE`[2] database of TDE light-curve parameters. This data set was compiled during the work presented in Mummery et al. (2024b), although since this publication more TDEs have been discovered, and some of these sources now have detectable late-time plateaus. We summarize the properties of the 14 new TDEs with detected late-time plateaus in Table 1 (see the tables in Appendix B for discovery references for each new TDE, and galactic properties). The remainder of our optical/UV sample is the

[2]All of this data are publicly available at https://github.com/sjoertvv/manyTDE.

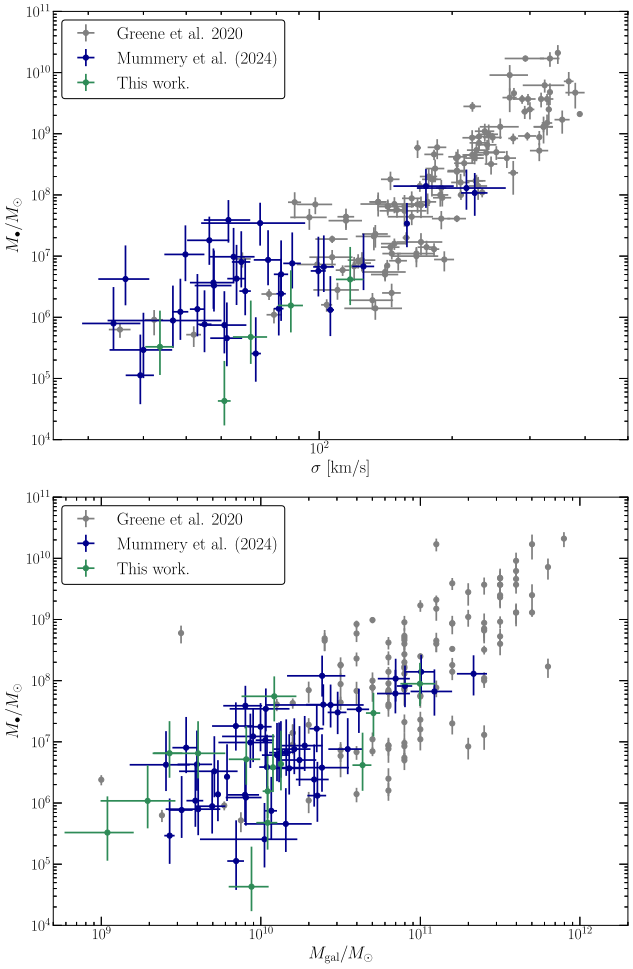

Figure 2. Updated $M_\bullet - \sigma$ (upper panel) and $M_\bullet - M_{\rm gal}$ (lower panel) scaling relationships including the new TDE measurements of Table 1. The (typically higher black hole mass) measurements are taken from the Greene et al. (2020) review, while the majority of the TDE population were first published in Mummery et al. (2024b). The new points remain consistent with the expected extrapolation of known relationships calibrated at higher masses.

data set presented in Mummery et al. (2024b). Owing to the continued collection of more data since publication some of these older TDEs now have subtly different plateau luminosity measurements.

The data reduction, and the process of plateau luminosity measuring, for each of these new TDEs follows exactly the procedure spelled out in Mummery et al. (2024b), their section 5. With the UV-plateau luminosity extracted, we can use the plateau luminosity–black hole mass scaling relationship to provide estimates of the black hole masses of each of these new TDEs. These masses are also presented (with 1σ uncertainties) in Table 1. Every TDE which is at a low redshift $z \leq 0.07$ and has at least 3 yr of data post-peak now has a detected optical/UV plateau, strongly suggesting that this is a ubiquitous property of TDE systems.

Many of the TDEs with plateau-inferred black hole masses also have independent estimates of their black hole masses from galactic scaling relationships, namely the velocity dispersion σ and galaxy mass $M_{\rm gal}$ relationships. In Fig. 2, we place the 14 new TDEs (not every TDE has a velocity dispersion measurement) onto the $M_\bullet - \sigma$ and $M_\bullet - M_{\rm gal}$ scaling relationships of Greene, Strader & Ho (2020). The new points remain consistent with the expected extrapolation of known relationships calibrated at higher masses. Note the systematically lower masses of the $M_\bullet - \sigma$ measurements of the newer population, this may be an example of Malmquist bias – those TDEs with fainter plateaus (a result of lower black hole masses) need more data to detect, and will in general be detected later in a survey.

In addition, we use the peak X-ray luminosity database collected in Guolo et al. (2024), and the peak g-band luminosity function presented in Yao et al. (2023). We have verified that the luminosity function presented in Yao et al. (2023) is consistent with that which would be inferred from our extended `manyTDE` data set.

3 ANALYSIS FRAMEWORK

It is the aim of this paper to reproduce the population-level properties of TDEs as observed at optical, UV, and X-ray frequencies. Theoretically, the reproduction of a distribution of 'observables' is a fundamentally rather simple two step process. First, one needs to specify the intrinsic distribution of physical TDE 'input' parameters (in this case the distributions of e.g. the black hole masses and spins, the stellar masses, etc., which are involved in these events). The second step is then turning each set of input parameters into a predicted 'output' observable (in our case these outputs are observed luminosities) using a physical model. In this section, we begin by introducing the physical model, then we discuss the functional form of the 'input' parameter distributions considered in this work, before concluding with a discussion of the raw data we are aiming to reproduce.

3.1 The relativistic accretion flow model

The fundamental physical model used in this work is the time-dependent relativistic accretion flow model which was developed in Mummery & Balbus (2020), and extended in Mummery et al. (2024b). This model is discussed in significant detail in the code paper (Mummery et al. 2024a), and in this paper we therefore only give a broad summary of its constituent components, and refer the reader to these earlier papers if more detail is required.

The model makes the assumption that one half of the disrupted stellar debris ultimately circularizes into an accretion flow, with initial radial scale given by the circularization radius of the disruption.[3] This disc material thereafter evolves according to the time-dependent general relativistic thin disc equation (Eardley & Lightman 1975; Balbus 2017), which is the relativistic analogue of the classical Lynden-Bell and Pringle Newtonian disc equation (Lynden-Bell & Pringle 1974). This governing equation evolves the disc density as a function of radius and time, from which the locally liberated photon flux of the disc can be computed. This local photon flux is assumed to be emitted quasi-thermally, with a temperature dependent colour-correction factor (Done et al. 2012) included to model disc opacity effects. For the sake of computational speed, we use the analytical disc solutions of Mummery (2023), which assume a vanishing innermost stable circular orbit (ISCO) stress for simplicity. This allows a rest-frame spectral energy distribution of the photons emitted from the accretion flow to be computed at every time post-disruption. The observer is assumed to be located at a distance D from the disc, orientated at an angle $\theta_{\rm obs}$ from the black hole's spin axis.

[3]The circularization radius is the radius at which one half of the stellar debris would settle if its initial parabolic orbit was transformed into a circular orbit while conserving angular momentum.

The observed spectral energy distribution of the emitted radiation is then computed using full relativistic ray-tracing calculations. We use a modified (Ingram et al. 2019; Mummery et al. 2024b) version of the publicly available code YNOGK (Yang & Wang 2013), which is based on GEOKERR (Dexter & Agol 2009) for the ray-tracing calculations. This observed spectral energy distribution can then be converted into observer frame light curves, which incorporate all relativistic effects. For a given set of input parameters, namely the black hole mass and spin $M_\bullet$, $a_\bullet$; the initial disc mass $M_{\rm disc}$ (taken to be one half of the incoming stellar mass); the 'viscous' evolutionary time-scale of the disc $t_{\rm visc}$, and observer inclination $\theta_{\rm obs}$, disc light curves can be produced at all frequency bands.

3.2 Physical parameter distributions

As discussed above, once a set of input parameters are specified, the output (luminosity at a given frequency versus time) of the disc model can be computed. At first glance, it may appear however that the parameter space available to fitting observed luminosity functions will be incredibly broad, and the problem will likely be underconstrained. Fortunately, however, nearly all of the key parameter distributions are known (to good approximation) a priori, as discussed in Mummery et al. (2024b). In this work, we fix the parameter distributions of all parameters except the black hole mass to that used in Mummery et al. (2024b). As an explicit example, the stellar mass distribution is fixed to that of the Kroupa (2001) initial stellar mass function, multiplied by the Wang & Merritt (2004) intrinsic stellar mass dependence of the TDE rate. We use the Kippenhahn & Weigert (1990) stellar mass–radius relationship throughout this work, so that only the stellar mass is a free parameter for a given disruption. We do not include any contribution to the TDE rate from red giants or white dwarfs. Other parameters are similarly simply distributed, we take flat (uninformative) prior distributions on the black hole spin parameter $a_\bullet$ for each black hole. We further assume that the observing inclination $\cos i$, and incoming stellar orbit angle $\sin\phi_{\rm orb}$ are uniformly distributed, as would be the case for an isotropic observer distribution (in the case of $\theta_{\rm obs}$) or isotropic galactic centre stellar population (in the case of $\phi_{\rm orb}$). In our sample we only include full disruptions (i.e. those with penetration factors $\beta \geq 1$), and sample the impact parameters according to the prescription of Stone & Metzger (2016) (see Mummery et al. 2024b, for more details).

To leading order therefore we have only one parameter distribution which must be fit from the data, the distribution of black hole masses in observed TDEs. In this work, we parametrize the TDE black hole mass distribution with the following functional form (Schechter 1976)

$$p_{M_\bullet}(m_\bullet) \propto \frac{m_\bullet^{\alpha_h}}{1+(M_c/m_\bullet)^{\alpha_l-\alpha_h}} \exp\left[-\left(\frac{m_\bullet}{M_g}\right)^{\gamma}\right]. \tag{1}$$

This represents a broken power law with a high-mass exponential cut-off. At low black hole masses ($M_\bullet \ll M_c$), this function is well approximated by a single power law with index $p_{M_\bullet} \sim m_\bullet^{\alpha_l}$, while for higher masses ($M_c \ll M_\bullet \ll M_g$) the power-law slope becomes $p_{M_\bullet} \sim m_\bullet^{\alpha_h}$, with the transition scale occurring at black hole masses $M_\bullet \sim M_c$. The very high mass behaviour is that of an exponential decay owing physically to the scarcity of high-mass galaxies. We take $M_g = 6.4 \times 10^7\,{\rm M}_\odot$ and $\gamma = +0.49$, which are the values presented in Shankar et al. (2004). Our results are only weakly sensitive to the values of γ and M_g, as the high-mass TDE rate is principally controlled by Hills mass suppression (discussed in detail in Appendix A), which leads to a superexponential rate suppression, rather than this exponential suppression. The aim of this analysis is to infer the parameters α_l, α_h, and M_c from TDE observations.

3.3 The optical/UV data

As was demonstrated in Mummery et al. (2024b), the properties of the late-time UV plateau observed in TDE light curves are well described by the relativistic accretion theory summarized above. It is this data set therefore which we use to constrain the parameters of the black hole mass distribution introduced above.

As discussed in Section 2, for the raw data we use the compilation of TDE late-time UV-plateau luminosities presented in Mummery et al. (2024b), with the addition of 14 new TDEs discovered since publication of this work. For each TDE with a late-time plateau, we also have a measured maximum optical luminosity, which will be used in later sections to compute the maximum observable volume of each source. The raw luminosity data are presented in Fig. 1, as an observed probability density function in the upper panel, and as an intrinsic rate in the lower panel. The intrinsic rate is computed by weighting the probability density function by the inverse of the observable volume of each source (see Appendix A for more details), so that harder to detect sources get a larger weight and are more accurately represented (i.e. this procedure accounts for Malmquist bias). The uncertainty in each rate value is given by the Poisson noise for the number of TDE sources which make up that bin.

In Appendix A, we construct a likelihood (denoted $\mathcal{L}$) which describes the probability of observing a given distribution of TDE UV-plateau luminosities, given a set of black hole mass distribution parameters $\{\xi\} = (\alpha_l, \alpha_h, M_c)$. This likelihood has the following functional form

$$\log \mathcal{L}\left(\{\xi\}\right) = \sum_{j=1}^{N_{\rm TDE}} \log p_L\left(L_j; \{\xi\}\right), \tag{2}$$

where L_j is the observed UV-plateau luminosity of the jth TDE in our sample. We do not weight the likelihood for each TDE, and therefore fit to the raw observed plateau luminosity distribution, rather than the intrinsic distribution. Importantly, this means that the parameters of the black hole mass distribution we constrain are for the observed TDE black hole mass distribution of our flux-limited sample, rather than the intrinsic black hole mass function.

The computation of the plateau luminosity probability density function $p_L(l)$, given a set of black hole mass distribution parameters, is the key step in this analysis, and is spelt out in detail in Appendix A, to which we refer the interested reader. Our sample comprises of $N_{\rm TDE} = 62$ sources with detected UV-plateau luminosities.

3.4 Statistical tests of the fit

We wish to contrast the predicted model luminosity functions with those which have been observed. In general, there are two statistical properties of the observed luminosity functions which we wish to recover. These are the observed cumulative luminosity distribution and the luminosity probability density functions (which formally contain the same information), and of course the intrinsic rate of the observed luminosities (the luminosity function itself). So as to be precise moving forward, we spend some time here defining each of these distributions in turn. The probability density function is defined by

$$p(\log L) = \frac{1}{N_{\rm TDE}} \frac{{\rm d}N_{\rm TDE}}{{\rm d}\log L}, \tag{3}$$

where L will represent either the UV plateau, optical peak, or X-ray peak luminosity. In other words, the probability density function is the unweighted and normalized histogram of the observed luminosity data. The normalization is simply defined so that

$$\int_{-\infty}^{+\infty} p(\log L)\,\mathrm{d}\log L = 1. \tag{4}$$

This probability density function allows us to define the cumulative distribution function of the data $\Phi(\log L)$

$$\Phi(\log L) = \int_{-\infty}^{\log L} p\left(\log L'\right)\,\mathrm{d}\log L'. \tag{5}$$

This is important because the cumulative distribution function allows non-parametric tests of goodness of fit to be performed, such as the two sample Kolmogorov–Smirnov (KS) test.

Finally the rate at which a given luminosity in our sample appears intrinsically is given by

$$\frac{\mathrm{d}\mathcal{R}}{\mathrm{d}\log L} \propto \frac{1}{\mathcal{V}(\log L)}\frac{\mathrm{d}N_{\rm TDE}}{\mathrm{d}\log L}, \tag{6}$$

where $\mathcal{V}$ is the maximum observable volume associated with each TDE.

The volume $\mathcal{V}$ can be simply estimated for our sample as we know how each TDE sample was constructed, namely from an optical survey telescope with a known flux detection limit, $F_{\rm lim}$ (although this analysis could also be performed for e.g. an X-ray instrument). In a Newtonian cosmology (which is a reasonable approximation for nearly all TDEs which are found at $z < 0.1$), the maximum distance out to which a source with given peak luminosity (optical or X-ray) $L_{\rm peak}$ can be observed is

$$D_{\rm max} \propto \sqrt{L_{\rm peak}} \tag{7}$$

and therefore an estimate of the volume out to which each TDE can be detected is (Appendix A for more discussion)

$$\mathcal{V} \propto D_{\rm max}^3 \propto \left(L_{\rm peak}\right)^{3/2}. \tag{8}$$

4 RESULTS

4.1 Black hole mass distribution

With the likelihood constructed, we can fit the three black hole mass distribution parameters α_l, α_h, and M_c to the UVplateau data using standard techniques. To be precise, we run a Monte Carlo Markov Chain (MCMC) analysis, using the EMCEE code (Foreman-Mackey et al. 2013). We use very broad, flat, and uninformative priors on our fitting parameters, namely $-5 < \alpha_l, \alpha_h < 5$, and $3 < \log M_c/\mathrm{M}_\odot < 10$. The posterior distributions of these three parameters are shown in Fig. 3.

As is clear in Fig. 3, this analysis is able to constrain both the high-mass slope α_h and turnover mass M_c, of the TDE black hole mass distribution. This approach, however, has effectively zero constraining power of the value of the low-mass slope α_l, owing to a lack of sources detected at very low luminosities. The only requirement picked out by the data is $\alpha_l > 0$, so that the TDE rate goes to zero at low masses. We caution against interpreting the large value of $M_c \sim 10^6\,\mathrm{M}_\odot$ as a fundamental change in the intrinsic black hole mass function at this scale, as it is possible that the high value is driven by the lack of observed plateau luminosities below $\log L_{UV,\rm plat} \lesssim 40.5$ (see Fig. 1). We cannot distinguish between an intrinsic and volume-limiting effect at this stage, a result we discuss further in Section 5. Current surveys do not necessarily have the required observable sensitivity to detect TDEs with plateau luminosities at this low level for the vast majority of our sources, and upper limits were found for some sources in the analysis of Mummery et al. (2024b), which we do not include in this work. We note however that the detection (or not) of a plateau for a given TDE was not found to correlate with galaxy mass (and therefore presumably black hole mass Mummery et al. 2024b). Future observational surveys with higher sensitivity will likely be able to overcome this effect, and determine if this represents a true turnover mass (if indeed such a mass scale exists) in the black hole mass function.

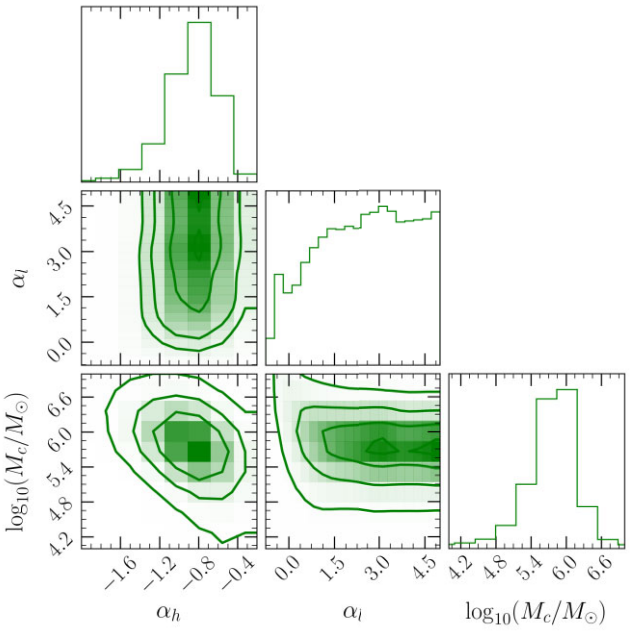

Figure 3. Posterior distributions of the black hole mass distribution parameters, resulting from a MCMC analysis of the TDE UV-plateau data. The data require a turnover in the TDE black hole mass rate at $M_\bullet \sim 10^6\,\mathrm{M}_\odot$ at high significance. This may be related to an intrinsic change in the black hole mass function, or could be driven by the lack of observing volume at these low luminosities, where current instruments do not typically have sensitivity. We cannot distinguish either scenario with current data.

This analysis finds $\alpha_h = -0.85 \pm 0.4$ (median $\pm$ standard deviation) and $\log M_c/\mathrm{M}_\odot = 5.8 \pm 0.8$. This suggests that the observed TDE population is dominated by black holes with masses $\sim 10^{6.5}\,\mathrm{M}_\odot$. It is interesting to note that this high-mass slope is statistically steeper than expected from extrapolated galactic scaling relationships and conventional models of the observed rate of TDEs on black hole mass (which would predict $\alpha_h \simeq 0$ for Eddington-limited accretion, e.g. Stone & Metzger 2016).

As a test of this analysis we compare the cumulative distribution function of the model black hole mass distribution with the observed black hole mass distribution, computed in three different manners (Fig. 4). These are from the $M_\bullet - M_{\rm gal}$ relationship (green step function, using the relationship of Greene et al. 2020), the $M_\bullet - \sigma$ relationship (red step function, using the relationship of Greene et al. 2020), and the $M_\bullet - L_{\rm plat}$ scaling relationship (blue step function, using the relationship of Mummery et al. 2024b). The model posterior median (purple curve) and 1σ uncertainty (purple shaded region), are also shown, with the effects of Hills mass suppression included (the effects of Hills mass suppression are discussed in more detail below). The posterior median model produces a formally acceptable description of both the $M_\bullet - M_{\rm gal}$ and $M_\bullet - L_{\rm plat}$ populations (we

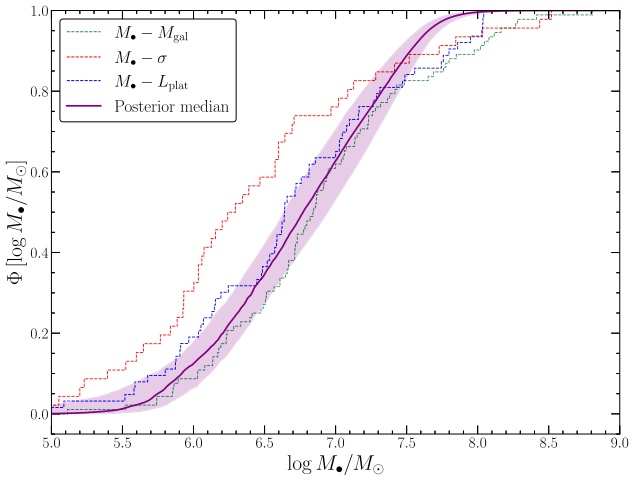

Figure 4. The cumulative distribution function of the observed TDE black hole masses of our sample, measured in three different ways. These are from the $M_\bullet - M_{\rm gal}$ relationship (green step function, Greene et al. 2020), the $M_\bullet - \sigma$ relationship (red step function, Greene et al. 2020), and the $M_\bullet - L_{\rm plat}$ scaling relationship (blue step function, Mummery et al. 2024b). The model posterior median (purple curve) and 1σ uncertainty (purple shaded region), are also shown, with the effects of Hills mass suppression included. The posterior median model produces a formally acceptable description of both the $M_\bullet - M_{\rm gal}$ and $M_\bullet - L_{\rm plat}$ populations, with the null hypothesis that the observed and simulated distributions are the same producing p-values > 0.1 for a two-sample KS test. The model is in contention with the $M_\bullet - \sigma$ population however (p-value $= 0.001$), see the text for further discussion.

cannot reject the null hypothesis that the observed and simulated distributions are the same). The model is in contention with the $M_\bullet - \sigma$ population however (p-value $= 0.001$).

This of course means that different scaling relationships are in contention with one another. Some of this tension is easy to understand physically: neither the $M_\bullet - M_{\rm gal}$ relationship or the $M_\bullet - \sigma$ relationship incorporate the effects of the Hills mass (whereas the plateau luminosity scaling relationship does), and therefore the deviations between the different scaling relationships at $M_\bullet \gtrsim 10^{7.5}\,{\rm M}_\odot$ are artificial. The origin of the discrepancy between the $M_\bullet - M_{\rm gal}$ and $M_\bullet - L_{\rm plat}$ relationships and the $M_\bullet - \sigma$ relationship at low black hole masses is less clear. We note that galactic scaling relationships have large intrinsic scatter (typically at least 0.5 dex), and so the smaller the sample (as in the case of σ measurements of which we have less than half of the number of $M_{\rm gal}$ measurements) the larger the uncertainty in the cumulative distribution function. Furthermore, the Greene et al. (2020) scaling relationships are calibrated on substantially larger black hole masses than the mass region of discrepancy (see e.g. Fig. 2), and it is unclear (physically, as well as empirically) whether these relationships potentially flatten at lower masses, which would remove this tension. As TDE sample sizes increase in the Rubin observatory era this will become an increasingly interesting question.

With the parameters of the black hole mass distribution constrained, we turn to the ability of this model to reproduce the observed luminosity functions, beginning with the plateau luminosity function.

4.2 The late-time UV-plateau distribution

As a first test of the theory, we compare the observed distributions of the UV-plateau luminosity, and the corresponding distributions predicted from the MCMC posterior median. Our results are displayed in Fig. 5.

The middle panel of Fig. 5 shows the observed plateau luminosity distribution in our sample (blue histogram and points), with model posterior shown by the purple curve and shaded region (median and 1σ uncertainty). To construct these curves, we sample $N = 10^5$ TDEs following the procedure described above, with α_l, α_h, and M_c set by their posterior median values (or sampled from the posterior distribution for each curve in the computation of the shaded region). The distribution of these 10^5 luminosities is then the predicted UV-plateau distribution. As can be seen in the middle and upper panels of Fig. 5, the fit is acceptable.

In the lowest panel in Fig. 5, we also display the (unnormalized) luminosity function of the UV-plateau population. The data are as in Fig. 1, and discussed above. The only slight change required to the theoretical distribution is to correct for $1/\mathcal{V}_{\rm max}$ in an analytical manner, which we do using the empirical peak optical luminosity–black hole mass scaling derived in Mummery et al. (2024b) (discussed in more detail later, see equation 9). In practice this corresponds to merely modifying each α_l, α_h when sampled by $\alpha_l, \alpha_h \to \alpha_l - 1.53, \alpha_h - 1.53$. This distribution provides an acceptable description of the observed UV-plateau luminosity function.

The fit to the probability density and cumulative distribution functions of the UV-plateau data is formally acceptable. The null hypothesis that the observed and simulated distributions are the same cannot be rejected by a two sample KS test (p-value $= 0.30$). This result gives us confidence in our disc theory approach, but the most important parts of this analysis relate to the implications of these results which are not part of the fit, e.g. the ability of this model to reproduce the X-ray luminosity distribution.

An example of one of these non-fitted results is shown in Fig. 6. In Fig. 6, we display the 2D black hole mass–plateau luminosity plane of our posterior median results. This was formed from a sample of $N = 10^6$ TDE systems following the procedure set out above. Each individual TDE sample is displayed by a grey point, with the blue curves showing 1σ, 2σ, and 3σ contours (i.e. they contain the central 68.2 per cent, 95.4 per cent, and 99.7 per cent of the simulated data, respectively). Also displayed are the observed TDE plateau luminosities, with black hole masses inferred from the galactic mass scaling relationship (we choose this rather than the velocity dispersion as not every TDE has a published velocity dispersion measurement). Note that the intrinsic scatter in each TDEs black hole mass measurement are not shown, and for the galactic mass scaling relationship this is of order 0.8 dex (Greene et al. 2020).

It is clear that the model put forward in this paper can reproduce not only the 1D distribution of the TDE plateau luminosity population (Fig. 5), but also the more detailed 2D mass-plateau luminosity plane (Fig. 6).

4.3 The peak X-ray luminosity distribution

The ability of a relativistic accretion disc model, coupled to a parametrized black hole mass distribution, to reproduce the observed TDE UV-plateau distribution is a promising result. More important however is the question of whether this same model can reproduce other, independent, observed properties of the TDE distributions, which are also expected to result from direct emission from accretion flows. This test is important because it would demonstrate that the physics of the model is correct, and the parameters of the black hole mass distribution which we obtained from a fit to the late-time UV luminosity distribution are in fact meaningful, and are not simply being overfit to the data.

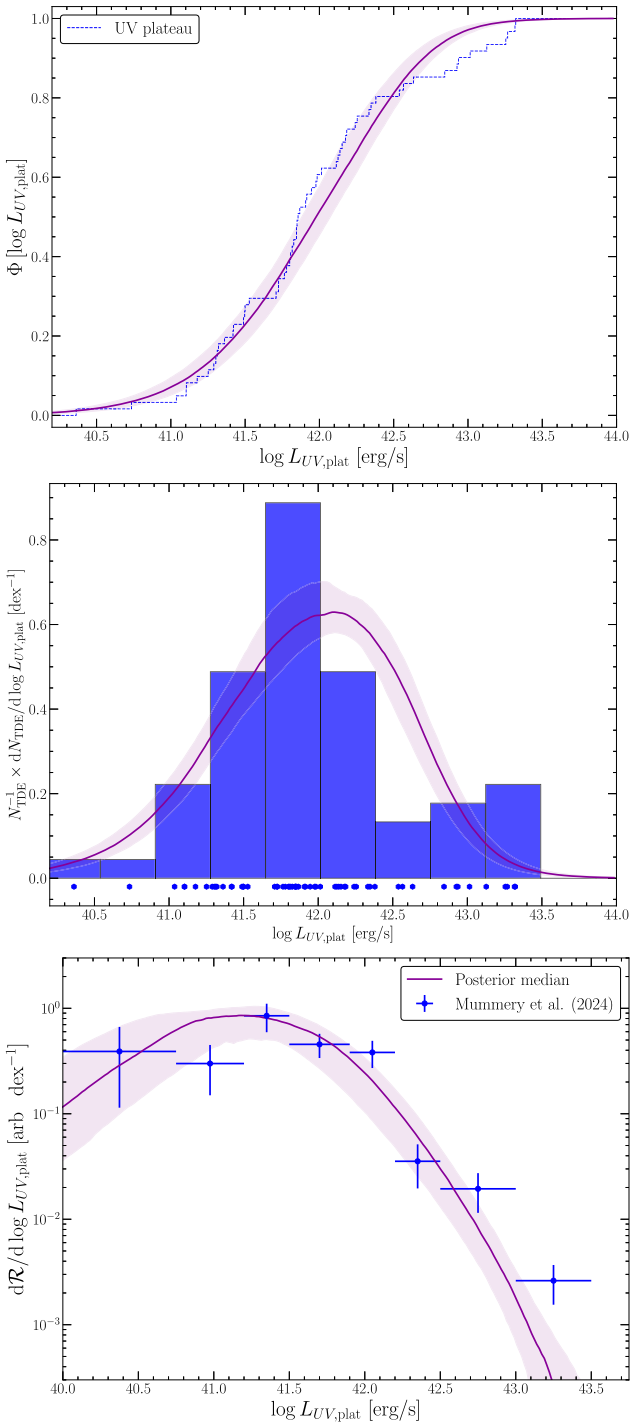

Figure 5. Lower: the luminosity function of the UV-plateau distribution, with each observation weighted by the volume associated with its peak optical luminosity (blue points). Also shown are the model predictions derived in this work (purple solid curve, with 1σ uncertainty shown by the shaded region). Middle: the probability density function (unweighted) of the observed UV-plateau luminosity sample (blue histogram; raw data shown by points), and posterior median (purple curve) and 1σ uncertainty (purple shaded region). Upper: the cumulative distribution function of the observed UV-plateau luminosity sample (blue step function) and the model posterior median (purple curve) and 1σ uncertainty (purple shaded region). The model produces an acceptable fit to the observed plateau luminosities. The null hypothesis that the observed and simulated distributions are the same cannot be rejected by a two sample KS test (p-value $= 0.30$).

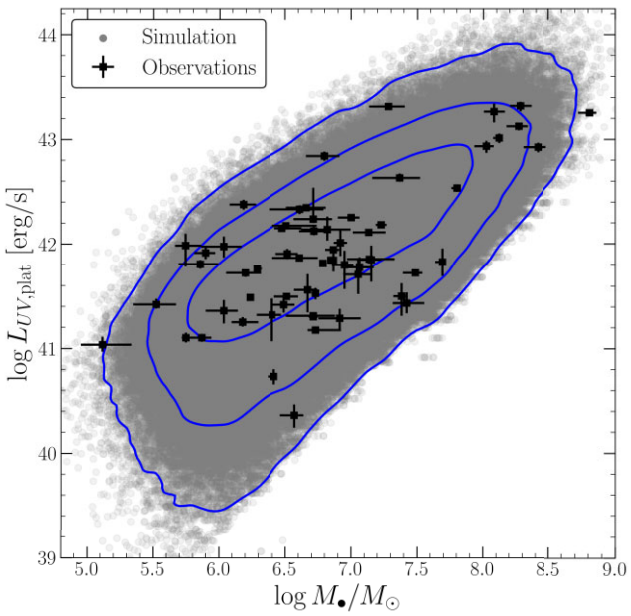

Figure 6. The 2D mass-plateau luminosity plane of the model derived here and observational data. In grey, we plot a sample of 10^6 theoretical TDEs, drawn from the posterior median black hole mass distribution, with the observational TDE data overplotted. Note that the intrinsic scatter in black hole measurements are not shown, and for the galactic mass scaling relationship this is of order 0.8 dex Greene et al. (2020). Blue contours show 1σ, 2σ, and 3σ, i.e. they contain the central 68.2 per cent, 95.4 per cent, and 99.7 per cent of the simulated data, respectively.

In addition to the late-time optical/UV luminosity of TDE systems, the X-ray luminosity of these systems is also thought to be powered by accretion, a framework successfully reproduces the data of numerous individual sources (Mummery & Balbus 2020; Wen et al. 2020, 2021; Mummery et al. 2023; Guolo et al. 2024). Indeed, the simultaneous reproduction of joint UV and X-ray properties is now routine (Mummery & Balbus 2020; Guolo et al. 2024). If both the model and statistical framework put forward in this work are correct, then this approach should naturally reproduce the X-ray luminosity function constructed in Guolo et al. (2024) with no further free parameters.

To perform this test, we numerically sample a large $N = 10^5$ sample of TDE X-ray luminosities (defined in this work as the integrated $0.3 - 10$ keV disc luminosity). We use the median probability density function for the black hole mass distribution ($N_{\rm TDE}^{-1}{\rm d}N_{\rm TDE}/{\rm d}\log M_\bullet$) obtained for the UV-plateau distribution, and resample sources following an identical procedure as spelled out in Mummery et al. (2024b) and Appendix A. We then further sample from the posterior distribution of α_l, α_h, and M_c, again sampling 10^5 X-ray TDEs each time, to construct a theoretical uncertainty in the X-ray luminosity distribution. For each sampled TDE, we then determine the peak X-ray luminosity (which is the most natural quantity to examine on the population level, and who's luminosity function was constructed by Guolo et al. 2024). All of the data used in this section are taken from Guolo et al. (2024), including the raw luminosities, the source designation (e.g. optically selected versus XMM slew), and X-ray luminosity function.

Some care must be taken at this point in this analysis, as at early times in the innermost disc regions relevant for X-ray observations (as opposed to the much later times and larger radii relevant for the UV plateau), some of the sampled systems may become formally

super-Eddington. At super-Eddington luminosities, the governing assumptions of the relativistic accretion theory employed in this work begin to break down, as the flow enters a so-called slim disc state (Abramowicz et al. 1988, see Wen et al. 2020 for an application of this model to TDEs). No out of temporal-equilibrium relativistic slim disc theory currently exists, as only steady-state theories have been developed. While a steady-state theory is unlikely to strictly correctly describe the properties of a TDE accretion flow near peak luminosity, as this is the evolutionary point at which the steady-state assumptions are maximally violated, steady-state theory does highlight a key piece of physics which can be incorporated into the thin disc theory used in this work. In a steady-state theory, an accretion flow is parametrized by a constant radial mass flux $\dot{m}$. For sub-Eddington accretion, the disc bolometric luminosity (normalized by the Eddington luminosity and denoted l) scales linearly with this accretion rate $l \propto \dot{m}$. Above the Eddington accretion rate however, an increase in $\dot{m}$ only results in a logarithmic increase in the emitted luminosity (Shakura & Sunyaev 1973), namely $l \propto \dot{m}_{\rm edd}(1 + \ln \dot{m})$. The physical reason for this transition from a linear to logarithmic increase is that the extra liberated energy above and beyond the Eddington limit is nearly all advected with the flow, rather than radiated away (energy advection is negligible in thin disc systems). As any apparent super-Eddington emission will in all likelihood be advected with the flow, it is a good approximation to treat the maximum bolometric luminosity of these sources as being fixed at the Eddington luminosity. We therefore compute the bolometric disc luminosity of each of our sampled systems, in addition to the $0.3 - 10$ keV X-ray luminosity. If the bolometric luminosity ever exceeds the Eddington, then the disc evolution is stopped (at a time we denote $t_{\rm edd}$), and the peak X-ray luminosity of this system is recorded at this time $L_{X,\rm peak} = L_X(t_{\rm edd})$. Otherwise, the peak X-ray luminosity is recorded as whatever maximum value the disc reaches during its evolution (this is typically at a time roughly one viscous time-scale into the evolution of the flow). This Eddington-limited framework was first proposed for TDE systems by Mummery (2021).

A key prediction made in Mummery (2021), was that this Eddington limiting (coupled with the emission of TDEs typically being in the Wien tail), would lead to an observable change in the X-ray luminosity distribution at the characteristic 'Eddington–Wien' luminosity scale $L_{X-\rm EW} \simeq 10^{44}$ erg s^{-1}, with significantly fewer sources detected with luminosities above this cut-off.

The results of this analysis, having followed the sampling procedure discussed above, are displayed in Fig. 7. To go from the sampled X-ray luminosity distribution to the intrinsic X-ray luminosity function it suffices to weight each system in our sample by $L_{X,\rm peak}^{-3/2}$ (to compensate for the Malmquist bias experienced by low-luminosity sources). The normalization of this rate is arbitrary (in our model), and was fit to match the amplitude of the Guolo et al. (2024) analysis.

As is clear from Fig. 7, relativistic disc theory is capable of reproducing the TDE X-ray luminosity function, from an original fit to the late-time UV luminosity function, with no additional free parameters. The null hypothesis that the observed and simulated distributions are the same cannot be rejected by a two sample KS test (p-value $= 0.41$). This is an extremely important result, as it demonstrates that the accretion flows which produce the late-time plateau observed in optical/UV bands are the very same accretion flows which produce the early-time X-ray luminosity observed in many systems.

The relevance of the Eddington–Wien upper luminosity limit can be clearly seen in both the probability density function of the peak X-ray luminosity population, and the TDE X-ray luminosity rate. In the raw observed distribution, there is a clear turnover in the observed

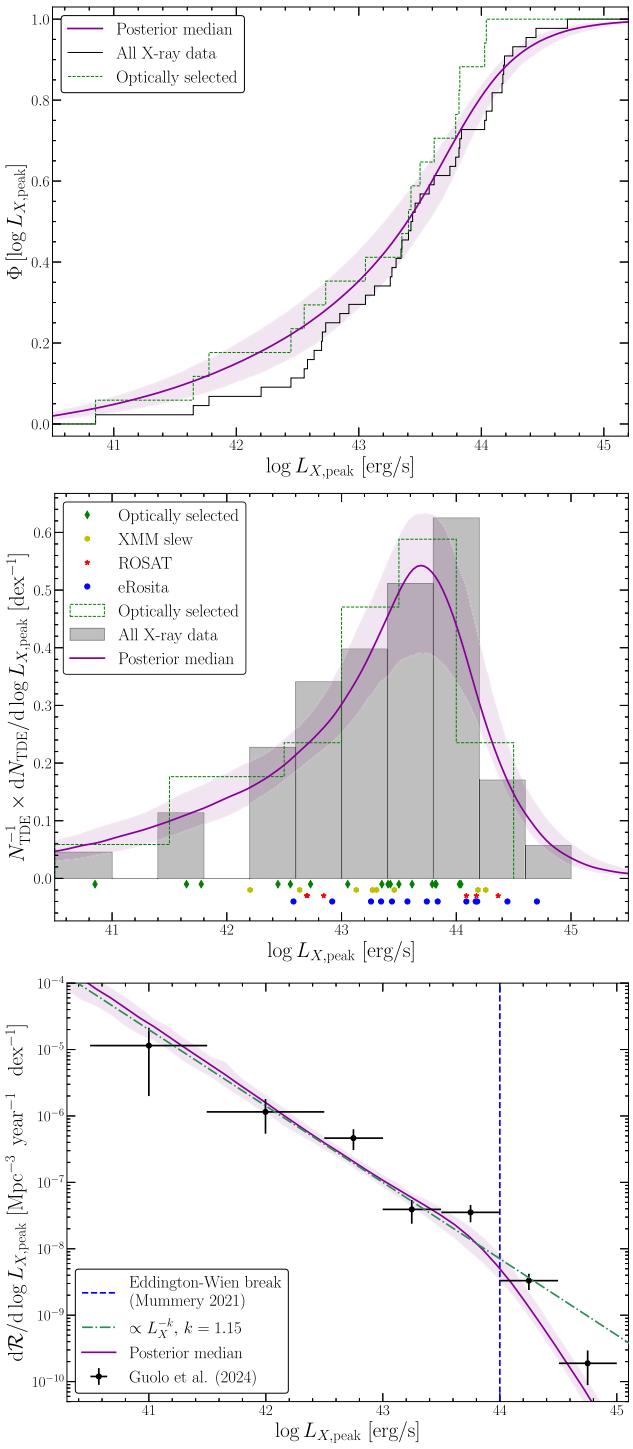

Figure 7. Lower: the inferred rate of the X-ray peak luminosities of the TDE population (black points), and the distribution predicted by the posterior fit to the UV-plateau data (purple line and 1σ shaded uncertainties). Middle: the probability density function (unweighted) of the observed peak X-ray luminosity sample (black histogram; raw data shown by individual points) coloured by detection method), and posterior median (purple curve and 1σ shaded uncertainties). Upper: the cumulative distribution function of the observed peak X-ray luminosity sample (black step function) and the model posterior (purple curve and 1σ shaded uncertainties). The model produces an excellent fit to all of the statistical properties of the data. The null hypothesis that the observed and simulated distributions are the same cannot be rejected by a two-sample KS test (p-value $= 0.41$).

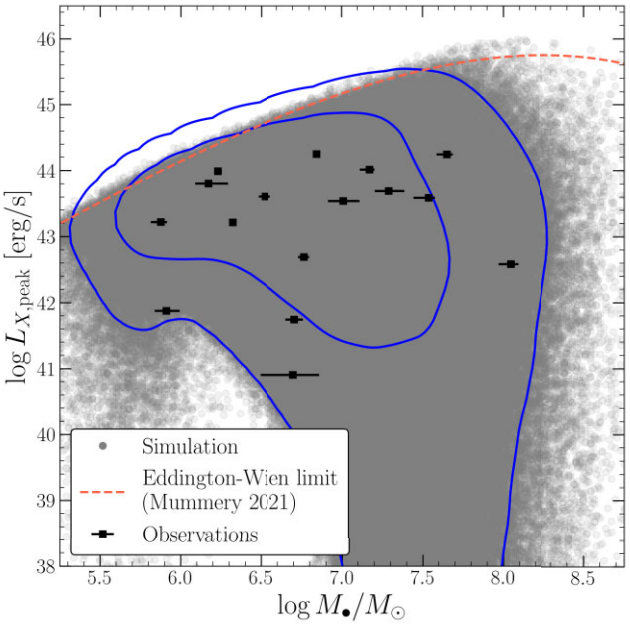

Figure 8. The 2D mass-peak X-ray luminosity plane of the model derived here and observational data. In grey, we plot a sample of 10^6 theoretical TDEs, drawn from the posterior median black hole mass distribution, with the observational TDE data overplotted. Note that the intrinsic scatter in black hole measurements are not shown, and for the galactic mass scaling relationship this is of order 0.8 dex Greene et al. (2020). Blue contours show 1σ and 2σ, i.e. they contain the central 68.2 per cent and 95.4 per cent of the simulated data respectively. The red-dashed curve shows the Eddington–Wien limiting luminosity derived in Mummery (2021).

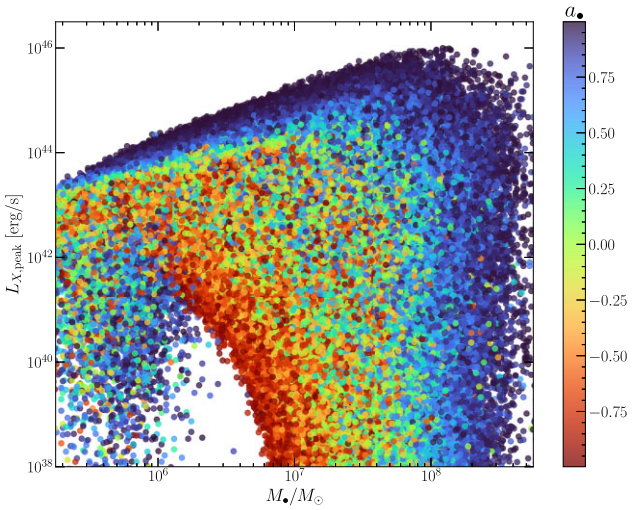

Figure 9. The 3D mass-peak X-ray luminosity–spin plane of the model derived here. By points we display a sample of $N = 10^6$ theoretical TDEs, drawn from the posterior median black hole mass distribution, with each point coloured by the spin parameter of the central black hole. Note that the relative density of points is much more difficult to ascertain in this figure, but can be identified with reference to Fig. 8. There are two key trends with black hole spin which can be seen here, the first is the increasing spin-dependent Hills mass allowing bright X-ray emission from more massive black holes (the left-to-right trend), while more rapidly spinning black holes produce brighter X-ray emission at all masses (the trend bottom to top). This plot does not show the relative density of systems at different mass/luminosity scales, which can be inferred from Fig. 8.

luminosity distribution at $L_{X-\mathrm{EW}} \simeq 10^{44}$ erg s^{-1}, while the peak X-ray luminosity rate displays a clear break at the same luminosity scale (as was first described empirically by Guolo et al. 2024, and recently also found in eROSITA data by Grotova et al. 2025). Below the break the peak X-ray luminosity rate (of both the data and model) can be well described by a power law of index $k \simeq -1.15$.

Unlike the earlier UV-plateau analysis, not every TDE in the Guolo et al. (2024) sample comes from an optical all-sky survey. In addition, not every observed TDE is comprehensively followed up with X-ray observations, and so it is natural to worry somewhat about combining different samples in this way. To examine if this survey combining has any effect on the strength of our results we can carry out an identical analysis using only those TDEs discovered in optical surveys (the green-dashed curves in Fig. 7). The null hypothesis that the observed and simulated distributions are the same in this case also cannot be rejected (a two sample KS test returns a p-value $= 0.62$).

Similarly, an identical analysis of those TDEs discovered only by X-ray surveys yields similar results. The null hypothesis that the observed and simulated distributions are the same in this case also cannot be rejected (a two sample KS test returns a p-value $= 0.14$).

This strength of this result can again be further emphasized by examining the 2D mass–luminosity plane of the theory and data. In Fig. 8, we display the 2D black hole mass–peak X-ray luminosity plane of our posterior median results. This was formed from a sample of $N = 10^6$ TDE systems following the procedure set out above. Each individual TDE sample is displayed by a grey point, with the blue curves showing 1σ and 2σ contours (i.e. they contain the central 68.2 per cent and 95.4 per cent of the simulated data, respectively). Also displayed are the observed optically selected TDE peak X-ray luminosities, with black hole masses inferred from the galactic mass scaling relationship (we choose this rather than the velocity dispersion as not every TDE has a published velocity dispersion measurement). Note that the intrinsic scatter in each TDEs black hole mass measurement are not shown, and for the galactic mass scaling relationship this is of order 0.8 dex (Greene et al. 2020).

These results strongly suggest that the optically and X-ray-selected population of TDEs are not distinct, but are drawn from the same overall distribution.

In addition, in Fig. 9, we display an interesting physical property of the X-ray luminosity of the TDE population. Fig. 9 shows the 3D mass-peak X-ray luminosity–spin plane of the model derived here. By points we display a sample of $N = 10^6$ theoretical TDEs (the same sample as in Fig. 8), drawn from the posterior median black hole mass distribution, with each point coloured by the spin parameter of the central black hole. Note that the relative density of points is much more difficult to ascertain in this figure, but can be identified with reference to Fig. 8. There are two key trends with black hole spin which can be seen here, the first is the increasing spin-dependent Hills mass allowing bright X-ray emission from more massive black holes (the left-to-right trend), while more rapidly spinning black holes produce brighter X-ray emission at all masses (the trend bottom to top). This contrasts interestingly with the UV-plateau luminosity (see fig. 5 of Mummery et al. 2024b), which is only sensitively to the Hills mass effect, not the intrinsic luminosity effect. Physically this results from the sensitivity of the X-ray luminosity in a TDE system to the temperature of the inner disc; this inner disc temperature is sensitive to the black hole spin parameter (more rapidly rotating black holes have a higher accretion efficiency η, and liberate more of the available accretion energy as photons).

Finally, we discuss the implications for our X-ray luminosity result in the context of different 'unification' schemes for understanding TDE emission (e.g. the reprocessing model of Dai et al. 2018). We note that we are able to reproduce the X-ray luminosity function, and observed distribution, of TDEs without requiring any absorption of X-ray photons along the line of sight between the disc and the observer. We also note that the optically selected and X-ray-discovered TDEs show near identical X-ray luminosity distributions (Fig. 7). At first glance, this seems to suggest that the early-time optical luminosity is not produced by the reprocessing (and therefore absorption) of X-ray photons from an accretion flow. However, we caution that there are other interpretations of this result. We cannot rule out that some fraction of TDEs yield X-ray non-detections purely as a result of absorption/reprocessing of X-ray photons, and we therefore reproduce the observed luminosity function as it contains only those sources which are not absorbed at all. In fact, roughly 3/4 of our TDE sample (i.e. 75 per cent of the systems sampled in producing Fig. 8) are predicted to be X-ray loud ($L_X \gtrsim 10^{42}$ erg s^{-1}), while only ~ 40 per cent of observed optically selected TDEs satisfy this criterion (Guolo et al. 2024), although this is of course a lower limit owing to incomplete X-ray follow up of optical TDEs. If this difference in X-ray brightness is in fact related to intrinsic physics, rather than observational selection effects, then we can envision three plausible interpretations of this result.

First, the reprocessing/absorption of X-ray photons (or whatever suppresses the X-ray luminosity in some cases) does occur for some TDE sources, but acts in an all-or-nothing fashion, either completely suppressing the X-ray luminosity of a TDE, or not at all. The reason this interpretation is permitted is that a more subtle change in X-ray luminosity of sources by reprocessing would alter the shape of the luminosity function itself (as opposed to simply reducing the amplitude, the result of removing some sources entirely). We believe this is the least likely of the three interpretations.

Alternatively, reprocessing is an important process for powering the early-time optical emission, but this reprocessing only suppresses the observed X-ray luminosity for a time-scale $t_{\rm sup}$ which is shorter than the typical time-scale over which the peak X-ray luminosity of the disc varies significantly. As the X-ray variation time-scale is of order a few 'viscous' time-scales, which can comfortably be of order $\mathcal{O}(100$'s) of days, this is certainly possible. This interpretation is supported by the findings of Guolo et al. (2024), which show a number of sources which appear to be dimmer at early times than expected from their emission observed at late times.

A third interpretation is that reprocessing of X-ray photons is not the physical mechanism by which the early-time optical emission is powered, and the difference between the 3/4 of sources predicted to be X-ray loud and the observed rate of ~ 40 per cent (if not selection effects) is due to some fraction of TDE sources failing to efficiently form an accretion flow in the earliest stages of their evolution. This may also explain the roughly $\sim 1/3$ of TDE systems which are (currently) not observed to transition to a plateau state in the optical/UV.

One way to test this going forward would be to examine TDEs with black hole masses $M_\bullet \lesssim 10^{6.0}\,{\rm M}_\odot$, with robust detections of discs at late times, which our model predicts would nearly always produce $L_X \gtrsim 10^{42}$ erg s^{-1} in an unabsorbed scenario (Fig. 8). If a black hole mass could be reliably inferred at this scale while a robust upper limit on the X-ray luminosity was found, this would imply either substantial absorption of X-ray photons or inefficient disc formation. Guolo et al. (2024) found that the black hole mass distribution of TDEs with $L_X \geq 10^{42}$ and $\leq 10^{42}$ erg s^{-1} are statistically indistinguishable, with both populations stretching down to $M_\bullet \sim 10^5\,{\rm M}_\odot$. On the other hand, our results (in the unabsorbed limit) would suggest that X-ray quiet ($L_X \leq 10^{42}$ erg s^{-1}) TDEs should be found around slightly higher black hole masses, and should certainly not extend down to $\sim 10^5\,{\rm M}_\odot$. While the results of Guolo et al. (2024) are based on a relatively small number ($N = 15$) of galactic scaling relationship black hole masses (which have substantial intrinsic scatter), this is suggestive that some TDEs are not producing any observable X-ray emission for some reason which is not related to the accretion flow itself. This result will be tested further as more TDEs (both X-ray bright and dim) are discovered in the future.

4.4 The early-time optical peak distribution

While the physical origin of the X-ray and late-time UV emission in TDEs are clear, the same is not true for the early-time optical emission observed in nearly all TDEs, which remains poorly understand. Current models either posit that the observed optical emission results from reprocessed accretion luminosity by a scattering atmosphere (e.g. Guillochon & Ramirez-Ruiz 2013; Dai et al. 2018), from the contraction of a radiation pressure-dominated cooling envelope (Metzger 2022), or from photon fluxes produced during debris streams shocking during the disc circularization process (e.g. Piran et al. 2015; Ryu, Krolik & Piran 2020). As there is no consensus on the physical origin of the early-time optical emission, we turn to the empirical scaling relationships derived using the results of disc theory first presented in Mummery et al. (2024b). The raw luminosity data used in this section were taken from Mummery et al. (2024b), while the g-band luminosity function was taken from Yao et al. (2023).

It is well known that the early-time optical luminosity in a TDE does not originate from the direct observation of an accretion flow. However, disc theory allows the black hole masses in a given disruption to be measured from the late-time UV-plateau luminosity. Using these masses, Mummery et al. (2024b) found an empirical relationship between peak g-band luminosity and black hole mass. This relationship is given by

$$\log L_{g,\rm peak}/{\rm erg\,s^{-1}} = 1.02 \log M_\bullet/{\rm M}_\odot + 36.35, \tag{9}$$

where we note the near-linear scaling suggests an Eddington-limited energy source.

A power-law relationship of this form allows a particularly simple calculation of the peak g-band luminosity function to be performed from our fitted black hole mass distribution, as

$$\frac{1}{N_{\rm TDE}}\frac{{\rm d}N_{\rm TDE}}{{\rm d}\log L_{g,\rm peak}} = \frac{1}{N_{\rm TDE}}\frac{{\rm d}N_{\rm TDE}}{{\rm d}\log M_\bullet} \times \frac{{\rm d}\log M_\bullet}{{\rm d}\log L_{g,\rm peak}}, \tag{10}$$

where the final factor is a simple constant, and the black hole mass distribution must be evaluated at the black hole mass which corresponds to the specified peak g-band luminosity (using equation 9). As we have already derived the black hole mass distribution using the UV-plateau data, this luminosity function is simple to compute. We can further compute the intrinsic peak optical g-band rate from

$$\frac{{\rm d}\mathcal{R}}{{\rm d}\log L_{g,\rm peak}} \propto \frac{1}{L_{g,\rm peak}^{3/2}}\frac{{\rm d}N_{\rm TDE}}{{\rm d}\log L_{g,\rm peak}}, \tag{11}$$

where we use equation (9) to evaluate the factor $L_{g,\rm peak}^{3/2}$.

The one non-trivial step in these calculations is to incorporate the effects of the Hills mass suppression at large black hole masses. We do this using TIDALSPIN, the publicly available code produced in Mummery (2024). This code convolves the naive g-band luminosity function derived above (which we denote $\bar{p}$) with the Hills

suppression factor $\mathcal{H}$

$$p(\log L_g) = \iiint \bar{p}(\log L_g)\mathcal{H}(a_\bullet, m_\star, \phi_{\rm orb}) \\ p(a_\bullet)p(m_\star)p(\phi_{\rm orb})\,{\rm d}a_\bullet\,{\rm d}m_\star\,{\rm d}\phi_{\rm orb}, \quad (12)$$

where $\mathcal{H} = 1$ if $M_\bullet < M_{\rm Hills}$ and $\mathcal{H} = 0$ if $M_\bullet \geq M_{\rm Hills}$. The Hills mass is presented explicitly in Appendix A. The three priors $p(a_\bullet)$, $p(m_\star)$, $p(\phi_{\rm orb})$ are identical to those used in the UV-plateau sampling procedure. The effect of the Hills mass suppression is visible in the lowest panel of Fig. 10, where we show by a red dotted line the peak g-band luminosity function in the absence of such an effect. The only modifications to the rate occur at high g-band luminosities (which correspond to the high black hole masses close to the Hills mass). The better agreement between the Hills-corrected luminosity function and the observational data can in some sense be taken as indirect evidence for the existence of event horizons in nature.

Similarly to the X-ray analysis, the normalization of the g-band luminosity rate is arbitrary (in our model), and was fit to match the amplitude of the Yao et al. (2023) analysis.

Just as with the peak X-ray and the UV-plateau luminosity functions, this procedure is capable of reproducing the observed peak optical luminosity function. The null hypothesis that the observed and simulated distributions are the same cannot be rejected by a two sample KS test with p-value $= 0.14$. This suggests that ultimately whatever is producing this early-time emission, while potentially physically very complicated as a process, must on the output emission level be relatively simple, as it can be adequately described on the population level by a single near-linear relationship between g-band luminosity and black hole mass.[4]

We note that, depending on how one calibrates the black hole masses of TDEs (i.e. with galactic scaling or the UV-plateau relationship), different peak luminosity–black hole mass scaling relationships are found (Pouw et al., in preparation). We have found that varying the peak–mass relationship between these different scaling relationship calibrations does not qualitatively affect the results presented here. Indeed, if one is only interested in reproducing the peak optical luminosity function, then a range of choices for a scaling $L_{\rm peak} = L_{\rm peak}(M_\bullet)$ can reproduce the data. If this change in peak luminosity relationship is chosen to be too far from $\sim$ linear however the black hole mass function must be modified, which will then put the predictions of this new theory in contention with the data in X-ray and (late-time) UV bands. The simultaneous reproduction of data in three different physical regimes is strongly constraining of the physics of the model.

We note in passing that a $\sim$ linear scaling between black hole mass and early-time peak luminosity (as is required by the data) is in contention with two commonly used models for this early emission. The TDEMass model Ryu et al. (2020, updated in Krolik, Piran & Ryu 2024) assumes $L_{\rm peak} \propto M_\bullet^{-1/6}\Xi(M_\bullet)^{5/2}$ (where $\Xi(M_\bullet)$ is a decreasing function of $M_\bullet$), which is in strong contention with the data. Similarly, MOSFiT's TDE model (Mockler, Guillochon & Ramirez-Ruiz 2019) assumes fallback-driven luminosities $L_{\rm peak} \propto \epsilon M_\bullet^{-1/2}$ which is also in strong contention with the data (unless the efficiency $\epsilon \sim M_\bullet^{3/2}$ which, as far as the authors are aware, is not expected on theoretical grounds). We note that the cooling envelope model of Metzger (2022) assumes Eddington-limited luminosities

[4]If this relationship was taken to be strictly linear, then the TDE g-band Eddington ratio would be $L_{g,{\rm peak}}/L_{\rm edd} \simeq 0.03$.

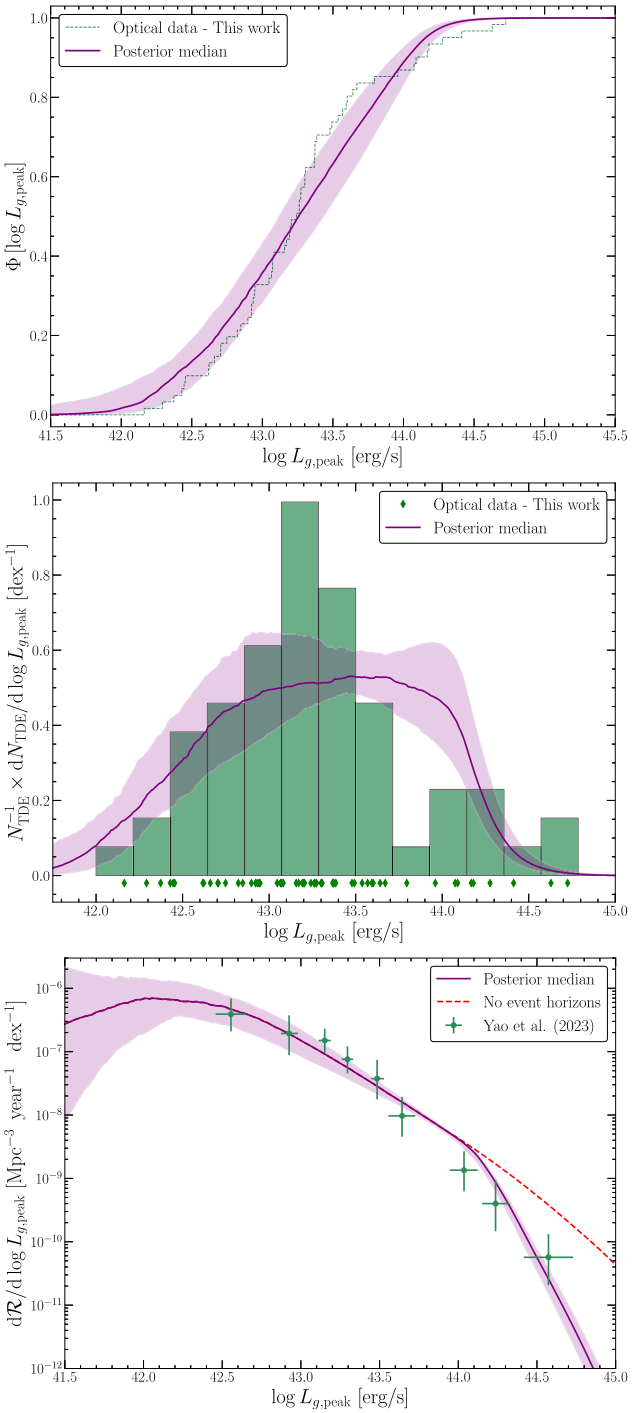

Figure 10. Lower: the inferred rate of the g-band peak luminosities of the TDE population (green points), and the distribution predicted by the posterior median fit the UV-plateau data (purple line). Middle: the probability density function (unweighted) of the observed peak g-band luminosity sample (green histogram; raw data shown by individual points), and posterior median (purple curve). Upper: the cumulative distribution function of the observed peak g-band luminosity sample (green step function) and the model posterior (purple curve). The model produces an excellent fit to all statistical properties of the data. The null hypothesis that the observed and simulated distributions are the same cannot be rejected by a two sample KS test p-value $= 0.14$. In the lower plot, we show the effects of the Hills mass suppression on the observed g-band luminosity rate, with the red-dashed curve showing the luminosity function if the presence of event horizons is neglected. 1σ model uncertainties in each plot are shown by a purple shaded region.

$L_{\rm peak} \propto M_\bullet$. While this is in no sense proof of that model, it is supportive.

5 IMPLICATIONS

5.1 Tidal disruption event science

We have demonstrated that it is possible to reproduce the TDE peak optical, late-time UV and peak X-ray luminosity functions from first principles using models of relativistic accretion flows. The first, and most obvious, implication of these results is that the physics of relativistic accretion is essential to understanding the observed distributions of TDE properties. The second key implication of this work is the demonstration that the accretion flows which produce the late-time plateaus observed in optical/UV bands are the very same accretion flows which produce the early-time X-ray luminosity observed in many of these systems.

There are, however, a number of other implications of these results, which we take some time to discuss here. First, this work demonstrates there is no 'missing energy' in TDE light curves. The so-called missing energy problem follows from the following observational statement, which was first discovered in the very early days of TDE surveys, that the integrated emitted energy in optical TDE light curves

$$E_{\rm opt} = \int_0^\infty L_{\rm opt}(t)\,{\rm d}t, \tag{13}$$

is significant lower than the mass-energy available in the stellar debris $\sim M_\star c^2$. Typically, $E_{\rm opt} \sim 10^{50}$ erg, while the formal energy budget is $M_\star c^2 \sim 10^{54}$ erg, naively suggesting a very low radiative efficiency. However, every disc model used in this paper accretes at least $M_{\rm acc} \geq 0.04\,{\rm M}_\odot$ (half of the lowest mass star in our stellar mass function), with the usual accretion efficiency η set exclusively by the black hole's spin. Ultimately therefore the solutions used in this work each release $\sim 10^{52}$ erg, as expected from simple energetic arguments. The vast majority of this radiated energy however is released in the form of (ultimately unobservable) extreme-UV photons, which will be absorbed by neutral Hydrogen on their path to the observer. Further, much of this energy is released on decade time-scales, not probed by the analysis of the (non-disc) early optical emission.

In addition, while the physics at the heart of the models put forward here is that of the accretion process, which does not directly describe the luminosity observed at early times in optical bands, our results have a number of implications for the true physical origin of this emission component. First, whatever its physical cause, the properties of this early-time optical emission must be relatively simple on the population level. This is because the observed g-band luminosity can be adequately described, on the population level, by a single near-linear relationship between g-band luminosity and black hole mass. Note that both commonly used TDE-fitting codes TDEMASS and MOSFIT have very different, negative, scalings between peak luminosity and black hole mass.

Furthermore, the model put forward in this paper is able to reproduce the peak X-ray luminosity distribution at the same time as reproducing the peak optical distribution. TDE X-ray light curves often peak at early times in the evolution of the system, when the early-time optical component is still bright (although the X-ray emission can sometimes be delayed, e.g. Guolo et al. 2024). Our results therefore seem, at first glance, to suggest that the early optical luminosity observed from these systems cannot be entirely explained by the reprocessing of X-ray emission to optical photons by a surrounding layer of material which persists for long (year) time-scales. However, reprocessing of X-ray emission does remain a viable model for the early-time optical emission. It does require that either (i) this reprocessing occurs over time-scales shorter than the time-scale at which the peak X-ray luminosity of the disc evolves substantially, or (ii) acts in an all-or-nothing fashion, as a more gradual change in X-ray luminosity (either caused by partial reprocessing or reprocessing on longer time-scales than the disc evolution) would alter the shape of the luminosity function (as opposed to simply reducing the amplitude at all luminosities, which appears to be the case). The authors believe option (i) is the more physically likely. A third possible resolution of this fact is of course that the early-time emission is not produced by the reprocessing of X-ray photons, but instead by either shocks in orbiting debris streams or perhaps by a scenario such as the 'cooling envelope' model of Metzger (2022).

We stress that our results are suggesting, however, that some TDEs are not producing any observable X-ray emission for some reason which is not related to the physical properties (e.g. the temperature) of the accretion flow itself. This is related to the fact that at masses $M_\bullet \lesssim 10^6\,{\rm M}_\odot$ our model predicts nearly every TDE should be X-ray loud $L_X \gtrsim 10^{42}\,{\rm erg\,s^{-1}}$, in contention with the finding of Guolo et al. (2024, although this was based on a small number of black hole mass measurements inferred from the $M_\bullet - \sigma$ relationship, and should be confirmed when larger data sets become available). Furthermore, 3/4 of our TDE sample (Fig. 8) are predicted to be X-ray loud ($L_X \gtrsim 10^{42}$ erg s^{-1}), while only ~ 40 per cent of observed optically selected TDEs satisfy this criterion (Guolo et al. 2024). An explanation of this result (first suggested in Guolo et al. 2024) is that some reprocessing is indeed occurring in some systems, which suppresses the amplitude of the X-ray emission at early times (this would also naturally explain the properties of some late X-ray brightening TDEs). Alternatively this may be a result of inefficient disc formation in some systems (see further discussion below), which may also explain the lack of a detected UV plateau in $\sim 1/3$ of sources (Mummery et al. 2024b), or of course this could simply be an observational selection effect (the 40 per cent figure found by Guolo et al. 2024, is by definition a formal lower limit in this regard).

Our final result relevant for TDE science is that our results suggest that the X-ray and optically selected TDE populations are drawn from the same mass distribution (as was also argued by Guolo et al. 2024, based on the $M_\bullet - \sigma$ masses of the two populations).

5.2 Black hole physics

In addition to the implications of these results for the physics of TDEs themselves, we are now at a point in TDE science where we can start to make statements regarding the intrinsic black hole mass distribution in the local Universe. The parametrized black hole mass distribution we fit in this work is displayed in Fig. 11, along with a volume-corrected distribution. This volume correcting incorporates a $1/\mathcal{V}_{\rm max} \propto L_{g,{\rm peak}}^{-3/2} \propto M_\bullet^{-1.53}$ factor to account for Malmquist bias [where we have used equation (9) for the peak g-band luminosities dependence on black hole mass]. In green, we display the observed black hole mass distribution, while in blue, we display this mass distribution once volume corrected. Red-dashed curves show the posterior median curves when the effects of the Hills mass suppression are not taken into account. We see that while there is a robust suppression in the observed TDE mass distribution below $10^6\,{\rm M}_\odot$, we cannot state with statistical significance that the volume-corrected mass distribution also shows a turnover at these lower masses. Future observations with surveys like Rubin/LSST

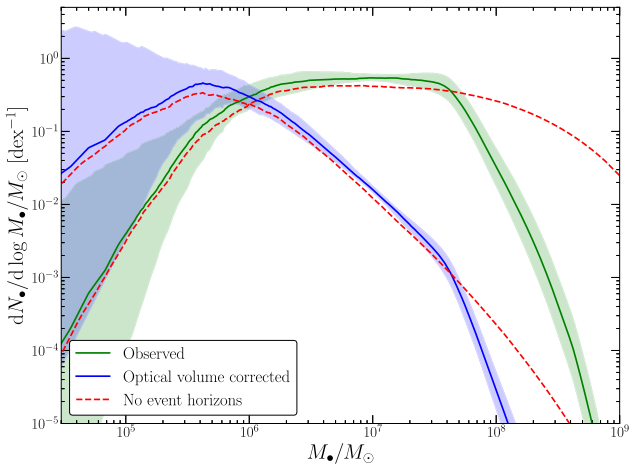

Figure 11. The black hole mass distributions implied by this work. In green, we display the observed black hole mass distribution, while in blue, we display this mass function once corrected for a simple Newtonian maximum observable volume effect (see the text for further discussion). In both situations, the solid curve shows the posterior median and the shaded region shows 1σ uncertainties. Red-dashed curves show the same posterior median curves when the effects of the Hills mass suppression are not taken into account. The normalizations of each curve are arbitrary, and were chosen so that the integral over all black hole masses of the green curves is unity. We see that while there is a robust suppression in the observed TDE mass distribution below 10^6 M$_\odot$, we cannot state with statistical significance that the volume-corrected mass distribution also shows a turnover at these lower masses. Future observations with surveys like Rubin/LSST will constrain the black hole mass function at these low masses.

will constrain the intrinsic black hole mass distribution at these low masses.

Note that this volume-corrected distribution still does not necessarily correspond to the intrinsic black hole mass function, as it does not take into account the intrinsic dependence of the TDE rate on black hole mass. This intrinsic rate, which we denote $\mathcal{R}_{\rm TDE}(M_\bullet)$ quantifies the differing rate at which black holes of different masses undergo TDEs, with all other parameters of the system fixed. This factor can have a non-trivial dependence on black hole mass if, for example, lower mass black holes were to typically reside in more central concentrated galaxies which naturally produce a higher rate of TDEs (the consensus within the community is that indeed they do, e.g. Wang & Merritt 2004). The quantity we are able to constrain in this work is the product $dN_\bullet/d\log M_\bullet \propto \mathcal{R}_{\rm TDE}(M_\bullet)\phi(M_\bullet)$, where $\phi(M_\bullet)$ is the intrinsic black hole mass function, a quantity of broad astrophysical interest. Most models for the mass dependence of $\mathcal{R}_{\rm TDE}$ are relatively weak, with (e.g. Alexander 2017; Yao et al. 2023) suggesting $\mathcal{R}_{\rm TDE} \propto M_\bullet^{-1/4}$, while Stone & Metzger (2016) suggest a slightly steeper $\mathcal{R}_{\rm TDE} \propto M_\bullet^{-2/5}$, and Pfister et al. (2020) suggest a slightly shallower $\mathcal{R}_{\rm TDE} \propto M_\bullet^{-0.14}$. Another important effect would be if the efficiency with which a given TDE is able to produce a disc (or indeed other emission components) varies systematically with black hole mass (this would introduce another implicit dependence in the rate $\mathcal{R}_{\rm TDE}$). As lower mass black holes have tidal radii further out in units of their gravitational radii, and therefore less precession of the stellar debris streams, disc formation may well be less efficient at lower black hole masses. Unless any of the above effects are particularly extreme, the intrinsic black hole mass function $\phi(M_\bullet)$ would be qualitatively unchanged from that shown in Fig. 11. More work (both on the physics of $\mathcal{R}_{\rm TDE}$, e.g. Hannah et al. 2024, and in extending the data sets used in this work) is required to confirm this result.

Naturally, our constraints on the black hole mass distribution and fits to the UV plateau are model dependent. It is interesting to ask if other models can reproduce the UV data, and thus produce potentially different mass distributions. As far as the authors are aware no other model, other than accretion disc emission, has been put forward to explain this late-time phase of TDE observations. The precise physical process by which the disc forms in a TDE does, however, impact the amplitude of this late-time UV emission. Recently, Krolik et al. (2024) have argued that a different disc formation scenario can explain the late-time UV emission. However, their predicted late-time UV scaling is $L_{\rm plat} \propto M_\bullet^{-1/2}\,\Xi(M_\bullet)^{3/2}$, where $\Xi(M_\bullet)$ is a moderately strongly decreasing function of black hole mass. Combined with the leading $1/\sqrt{M_\bullet}$ factor this therefore predicts a strongly decreasing plateau luminosity as a function of black hole mass. The observational data of the late-time UV luminosity shows a highly statistically significant positive dependence on the black hole mass (these masses are inferred from galactic scaling relationships), with a power-law index $\approx +2/3$ (Mummery et al. 2024b). The Krolik et al. (2024) disc formation scenario is therefore in strong contention with observations of TDEs, and we believe our results are robust against this model systematic.

6 CONCLUSIONS

The key result of this paper is that the optical (Fig. 10), UV (Fig. 5), and X-ray (Fig. 7) properties of TDEs can now be accurately described on the population level by using time-dependent relativistic models of accretion flows. The three free parameters fit in this work describe the observed TDE black hole mass distribution, and are of astrophysical interest (e.g. Fig. 11).

The mass and luminosity functions derived here will be of further use for predicting the future properties of (e.g.) the optical/UV TDE population discovered by Rubin/LSST (which is predicted to discover tens of thousands of TDEs, e.g. Bricman & Gomboc 2020), or the X-ray properties of TDEs discovered by the Einstein probe (which is expected to discover a similar number to LSST; Yuan et al. 2015). If future, better sampled, observational data sets provide even tighter constraints on the black hole mass function at the low-mass end then this could have profound implications for the future Laser Interferometer Space Antenna (LISA) binary black hole detection rate (Amaro-Seoane et al. 2017).

The statistical framework developed in this paper can be extended more broadly to constrain other parameters of TDE systems. Of particular interest would be future black hole spin constrains which can be determined by the delicate interplay between observed TDE parameters and the Hills mass (e.g. Mummery 2024).

DATA ACCESSIBILITY STATEMENT

All optical/UV light curves and data products are available in the following repository: https://github.com/sjoertvv/manyTDE. The X-ray luminosity data were taken from Guolo et al. (2024), andares publicly available. The peak optical luminosity function was taken from Yao et al. (2023), and is publicly available. The base FitTeD code package used in this work is available to download at the following repository: https://bitbucket.org/fittingtransientswithdiscs/fitted_public/src.

ACKNOWLEDGEMENTS

The authors would like to thank E. Rossi and N. Stone for illuminating discussions during the early stages of this work. This work was supported by a Leverhulme Trust International Professorship grant [no. LIP-202-014]. For the purpose of Open Access, AM has applied a CC BY public copyright licence to any Author Accepted Manuscript version arising from this submission. This research was supported in part by grant no. NSF PHY-2309135 to the Kavli Institute for Theoretical Physics (KITP).

REFERENCES

Abramowicz M. A., Czerny B., Lasota J. P., Szuszkiewicz E., 1988, ApJ, 332, 646
Alexander T., 2017, ARA&A, 55, 17
Amaro-Seoane P. et al., 2017, preprint (arXiv:1702.00786)
Arcavi I. et al., 2022a, Transient Name Server Classification Report, 2022-504, 1
Arcavi I., Dgany Y., Pellegrino C., Howell D. A., Burke M. N. J., Gonzalez E. P., Terreran G., McCully C., 2022b, Transient Name Server Classification Report, 2022-511, 1
Balbus S. A., 2017, MNRAS, 471, 4832
Bricman K., Gomboc A., 2020, ApJ, 890, 73
Charalampopoulos P. et al., 2024, A&A, 689, A350
Dai L., McKinney J. C., Roth N., Ramirez-Ruiz E., Miller M. C., 2018, ApJ, 859, L20
Dexter J., Agol E., 2009, ApJ, 696, 1616
Done C., Davis S. W., Jin C., Blaes O., Ward M., 2012, MNRAS, 420, 1848
Eardley D. M., Lightman A. P., 1975, ApJ, 200, 187
Esquej P. et al., 2008, A&A, 489, 543
Foreman-Mackey D., Hogg D. W., Lang D., Goodman J., 2013, PASP, 125, 306
Fulton M. et al., 2022a, Transient Name Server AstroNote, 106, 1
Fulton M., Smith K. W., Moore T., Srivastav S., Bruch R. J., 2022b, Transient Name Server Classification Report, 2022-584, 1
Greene J. E., Strader J., Ho L. C., 2020, ARA&A, 58, 257
Grotova I. et al., 2025, A&A, 697, A159
Guillochon J., Ramirez-Ruiz E., 2013, ApJ, 767, 25
Guolo M., Gezari S., Yao Y., van Velzen S., Hammerstein E., Cenko S. B., Tokayer Y. M., 2024, ApJ, 966, 160
Hammerstein E., Gezari S., Velzen S. V., Kulkarni S., Cenko B., Yao Y., 2021a, Transient Name Server Classification Report, 2021-732, 1
Hammerstein E., Gezari S., Velzen S. V., Kulkarni S., Cenko B., Yao Y., 2021b, Transient Name Server Classification Report, 2021-732, 1
Hammerstein E., Yao Y., Gezari S., Velzen S. V., Somalwar J., Cenko B., 2022, Transient Name Server Classification Report, 2022-891, 1
Hannah C. H., Seth A. C., Stone N. C., van Velzen S., 2024, AJ, 168, 137
Holoien T. W. S. et al., 2016, MNRAS, 455, 2918
Ingram A., Mastroserio G., Dauser T., Hovenkamp P., van der Klis M., García J. A., 2019, MNRAS, 488, 324
Kippenhahn R., Weigert A., 1990, Stellar Structure and Evolution, Springer-Verlag, Berlin, Heidelberg, New York
Krolik J., Piran T., Ryu T., 2024, preprint (arXiv:2409.02894)
Kroupa P., 2001, MNRAS, 322, 231
Lynden-Bell D., Pringle J. E., 1974, MNRAS, 168, 603
Magorrian J., Tremaine S., 1999, MNRAS, 309, 447
Metzger B. D., 2022, ApJ, 937, L12
Mockler B., Guillochon J., Ramirez-Ruiz E., 2019, ApJ, 872, 151
Mummery A., 2021, MNRAS, 504, 5144
Mummery A., 2023, MNRAS, 518, 1905
Mummery A., 2024, MNRAS, 527, 6233
Mummery A., Balbus S. A., 2020, MNRAS, 492, 5655
Mummery A., Nathan E., Ingram A., Gardner M., 2024a, preprint (arXiv:2408.15048)
Mummery A., van Velzen S., Nathan E., Ingram A., Hammerstein E., Fraser-Taliente L., Balbus S., 2024b, MNRAS, 527, 2452
Mummery A., Wevers T., Saxton R., Pasham D., 2023, MNRAS, 519, 5828
Nicholl M. et al., 2019, MNRAS, 488, 1878
Pfister H., Volonteri M., Dai J. L., Colpi M., 2020, MNRAS, 497, 2276
Piran T., Svirski G., Krolik J., Cheng R. M., Shiokawa H., 2015, ApJ, 806, 164
Rees M. J., 1988, Nature, 333, 523
Ryu T., Krolik J., Piran T., 2020, ApJ, 904, 73
Sazonov S. et al., 2021, MNRAS, 508, 3820
Schechter P., 1976, ApJ, 203, 297
Shakura N. I., Sunyaev R. A., 1973, A&A, 24, 337
Shankar F., Salucci P., Granato G. L., De Zotti G., Danese L., 2004, MNRAS, 354, 1020
Somalwar J. J. et al., 2025, ApJ, 982, 163
Stone N. C., Metzger B. D., 2016, MNRAS, 455, 859
van Velzen S. et al., 2019a, ApJ, 872, 198
van Velzen S. et al., 2021, ApJ, 908, 4
van Velzen S., Stone N. C., Metzger B. D., Gezari S., Brown T. M., Fruchter A. S., 2019b, ApJ, 878, 82
Wang J., Merritt D., 2004, ApJ, 600, 149
Wen S., Jonker P. G., Stone N. C., Zabludoff A. I., 2021, ApJ, 918, 46
Wen S., Jonker P. G., Stone N. C., Zabludoff A. I., Psaltis D., 2020, ApJ, 897, 80
Wevers T. et al., 2021, ApJ, 912, 151
Wevers T., Guolo M., Pasham D. R., Coughlin E. R., Tombesi F., Yao Y., Gezari S., 2024, ApJ, 963, 75
Yang X., Wang J., 2013, ApJS, 207, 6
Yao Y. et al., 2023, ApJ, 955, L6
Yao Y., Graham M., Rodriguez A., Somalwar J., Velzen S. V., Gezari S., Hammerstein E., 2022, Transient Name Server Classification Report, 2022-620, 1
Yuan W. et al., 2015, preprint (arXiv:1506.07735)

APPENDIX A: STATISTICAL FORMALISM

In this appendix, we shall introduce and formalise the statistical procedure used in this paper to derive constraints on the black hole mass distribution of those black holes represented in the TDE population. In deriving this formalism it will prove most useful to consider a more general approach than is strictly required for the present calculations, as the procedure used in this paper can be generalized to study the distributions of other key parameters (i.e. the stellar properties of the TDE population), this may be of interest in the future when more data are available.

To keep this formalism general, let us suppose there is a function f which returns a TDE observable L from a set of physical input parameters $\{\Psi\}$, i.e.

$$L = f(\{\Psi\}). \tag{A1}$$

The notation L is used here as the observable is most likely to be some observed luminosity (but in principle this could be any quantity), and the list of input parameters is formally completely general but is likely to be (at least for the accretion problem at hand)

$$\{\Psi\} = [M_\bullet, a_\bullet, M_\star, R_\star, \theta_{\rm obs}, \phi_{\rm orb}, \alpha, \beta, \dots]. \tag{A2}$$

Here notation is completely standard: $M_\bullet$, $a_\bullet$ are the black hole mass and spin; $M_\star$, $R_\star$ the stellar mass and radius; $\theta_{\rm obs}$ is the disc–observer inclination, and $\phi_{\rm orb}$ is the angle made between the incoming stellar orbit and the black hole's spin axis (which is an important parameter for determining the Hills mass); α represents the classical disc turbulence parameter of Shakura & Sunyaev (1973); while β is the impact parameter. Naturally, this list could be extended if required (e.g. to include stellar metalicity, etc.).

Further suppose that the probability distributions of each of our parameters is known (or at least a suitable parametrized distribution

can be written down). We will use the following notation for all probability density functions: $p_X(x)\mathrm{d}x$ is the probability that variable X takes a value in the range $x \to x + \mathrm{d}x$. It follows that the probability density function for our observable L is given by

$$p_L(l) \propto \iint\!\!\dots\!\int p_\Psi(\psi)\,\delta\left(l - f(\psi)\right)\,\mathrm{d}^N\psi, \tag{A3}$$

where the integral is over all N variables in the list $\{\Psi\}$, and the function $p_\Psi(\psi)$ is the joint probability density function of the N variables. The normalization of this proportionality, which is not required for the calculation at hand, is given by the same integral as above but with an additional integration over all observables l. In words, this simply states that the probability of observing a given value l of the observable L is the sum of all possible ways of obtaining that value l with different input parameters, weighted by the relative probabilities of those input parameters occurring. To be explicit, for a TDE this would look something like (where '…' indicate other possible parameters to be marginalized over)

$$\begin{aligned} p_L(l) \propto \int p_{M_\bullet}(m_\bullet)\int p_{A_\bullet}(a_\bullet)\int p_{M_\star}(m_\star)\int p_{\Theta_{\rm obs}}(\theta_{\rm obs})\int p_{\Phi_{\rm orb}}(\phi_{\rm orb})\dots \\ \Theta\left(M_{\rm hills}(a_\bullet, m_\star, \phi_{\rm orb}, \dots) - m_\bullet\right)\delta\left(l - f(m_\bullet, a_\bullet, m_\star, \theta_{\rm obs}, \dots)\right) \\ \times\,\mathrm{d}m_\bullet\,\mathrm{d}a_\bullet\,\mathrm{d}m_\star\,\mathrm{d}\theta_{\rm obs}\,\mathrm{d}\phi_{\rm orb}\dots \end{aligned} \tag{A4}$$

The above integral introduces the first non-trivial point of statistics regarding the TDE calculation. Even if the parameter distributions of (e.g.) black hole masses and spins are independent in the wider universe they become fundamentally coupled when considering TDEs as only certain sets of parameters – those which produce a tidal radius outside of the event horizon – are observable (the fact that the statistical independence of black hole masses and spins is unlikely to be true in nature is beside the point). This coupling can be simply modelled by the inclusion of a Heaviside theta function, defined as

$$\begin{aligned} &\Theta\left(M_{\rm hills}(a_\bullet, m_\star, \phi_{\rm orb}, \dots) - m_\bullet\right) \\ &\quad= \begin{cases} 1, & \text{if } M_{\rm hills}(a_\bullet, m_\star, \phi_{\rm orb}, \dots) > m_\bullet, \\ 0, & \text{if } M_{\rm hills}(a_\bullet, m_\star, \phi_{\rm orb}, \dots) \leq m_\bullet. \end{cases} \end{aligned} \tag{A5}$$

The so-called Hills mass $M_{\rm Hills}$ represents the limiting black hole mass at which (for a given stellar mass and radius) the tidal disruption occurs precisely at the point at which all of the debris is immediately lost within the event horizon (and therefore no observable emission can be detected). The Hills mass can be derived analytically in the Kerr metric, as was recently shown by Mummery (2024), and is given by

$$\begin{aligned} M_{\rm Hills}(a_\bullet, \phi_{\rm orb}, M_\star, R_\star) = \left[\frac{2R_\star^3 c^6}{G^3 M_\star}\right]^{1/2}\frac{1}{\chi^{3/2}} \\ \times\left[1 + \frac{6\chi}{\chi^2 - a_\bullet^2\cos^2\phi_{\rm orb}} + \frac{3a_\bullet^2}{2\chi^2} - \frac{6a_\bullet\sin\phi_{\rm orb}}{\sqrt{\chi^3 - a_\bullet^2\chi\cos^2\phi_{\rm orb}}}\right]^{1/2}, \end{aligned} \tag{A6}$$

where $\chi(a_\bullet, \phi_{\rm orb})$ is the root of

$$\begin{aligned} &\chi^4 - 4\chi^3 - a_\bullet^2(1 - 3\cos^2\phi_{\rm orb})\chi^2 + a_\bullet^4\cos^2\phi_{\rm orb} \\ &\quad + 4a_\bullet\sin\phi_{\rm orb}\sqrt{\chi^5 - a_\bullet^2\chi^3\cos^2\phi_{\rm orb}} = 0. \end{aligned} \tag{A7}$$

Including a Heaviside theta function in this manner allows each parameter integral to be performed independently. This is done for convenience for later steps and does not affect the statistical formalism.

Now, as written the probability density function of each variable only depends on the value that variable takes. This would be true if we had a perfect description of the underlying distributions, with no tuneable parameters. Of course, in reality, we are in fact interested only in the values that these tuneable parameters take. To bring this formalism back in line with the main body of the paper we shall use the black hole mass distribution as an explicit example. The simple functional form of the black hole mass distribution used in this work is

$$\begin{aligned} &p_{M_\bullet}(m_\bullet; \alpha_h, \alpha_l, M_c, M_g, \gamma) \\ &\quad\propto \frac{m_\bullet^{\alpha_h}}{1 + (M_c/m_\bullet)^{\alpha_l - \alpha_h}}\exp\left(-\left(\frac{m_\bullet}{M_g}\right)^\gamma\right). \end{aligned} \tag{A8}$$

The point being that in reality each of our probability density functions has tuneable parameters (α_h, α_l, M_c, M_g, and γ in the above), and our probability density function for our observable L is a function of only these parameters. Call the list of all tuneable parameters $\{\xi_i\}$, then

$$p_L(l, \{\xi_i\}) \propto \iint\!\!\dots\!\int p_\Psi(\psi, \{\xi_i\})\,\delta\left(l - f(\psi)\right)\,\mathrm{d}^N\psi. \tag{A9}$$

This construction allows us to determine $\{\xi_i\}$ given a set of observations $\{L_j\}$. By definition, the likelihood of observing $\{L_j\}$ is

$$\mathcal{L}\left(\{\xi_i\}\right) = \prod_{j=1}^{N_{\rm TDE}} p_L\left(L_j, \{\xi_i\}\right), \tag{A10}$$

which is a function only of $\{\xi_i\}$ (i.e. the likelihood is formally the probability of observing the set $\{L_j\}$ given a probability density function $p_L(l, \{\xi_i\})$). Of course one should work with the log likelihood as this is much less likely to be affected by numerical rounding errors

$$\log\mathcal{L}\left(\{\xi_i\}\right) = \sum_{j=1}^{N_{\rm TDE}}\log p_L\left(L_j, \{\xi_i\}\right). \tag{A11}$$

Then, given a set of observations $\{L_j\}$, the maximum-likelihood estimation of the underlying tuneable parameters $\{\xi_i\}$ is just

$$\{\xi_\star\} = \max_{\{\xi_i\}}\left[\log\mathcal{L}\left(\{\xi_i\}\right)\right]. \tag{A12}$$

The parameter set $\{\xi_\star\}$ is of obvious astrophysical interest, and is what we solve for in this work.

A1 Weighted likelihood

The likelihood constructed above will, when suitably maximized, return the tuneable parameters $\{\xi_i\}$ which best describe the observed distribution of tidal disruption parameters. While this is the quantity which we work with in this paper it is not always the distribution of most interest. For other applications, we are often more interested in the parameter distribution which best describes the true intrinsic rate at which different TDE properties occur in the wider Universe, and not the subset of which we are ultimately able to observe. To complete the statistical formalism presented in this appendix, we describe how that approach would be performed.

To constrain the intrinsic distribution the likelihood derived above must be reweighted, in the following manner. With each TDE in our sample we can associate a volume $\mathcal{V}_j$, which is given by the maximum volume out to which this particular TDE could have

been observed. Naturally, sources with larger/smaller $\mathcal{V}_j$ will be over/under-represented in our sample, compared to their true intrinsic rates. The likelihood therefore must, if the goal is to understand the intrinsic rates of properties of TDEs, be weighted by the inverse source volume of each TDE. Defining $\widehat{\mathcal{L}}$ as this weighted likelihood, the weighting must be performed in the following manner

$$\widehat{\mathcal{L}}\left(\{\xi_i\}\right) = \prod_{j=1}^{N_{\rm TDE}} \left[p_L\left(L_j, \{\xi_i\}\right)\right]^{w_j}, \tag{A13}$$

where $w_j \propto 1/\mathcal{V}_j$. In words, the mathematical reason for this is that a source in our sample with a volume 1/8th of another will in reality occur eight times as frequently in the global population (and should therefore be counted eight times). In log-space we therefore have

$$\log \widehat{\mathcal{L}}\left(\{\xi_i\}\right) = \sum_{j=1}^{N_{\rm TDE}} w_j \log p_L\left(L_j, \{\xi_i\}\right). \tag{A14}$$

The volume $\mathcal{V}_j$ can be simply estimated for each source in our sample as our TDE population is constructed from optical survey telescopes, with a known flux detection limit, $F_{\rm lim}$. In a Newtonian cosmology (which is a reasonable approximation for nearly all TDEs which are found at $z \lesssim 0.1$, although we note that our most luminous TDEs are observed out to $z \sim 0.3$), the maximum distance out to which a source with peak optical luminosity $L_{g,{\rm peak},j}$ can be observed is

$$D_{\rm max} = \sqrt{\frac{L_{g,{\rm peak},j}}{4\pi F_{\rm lim}}}. \tag{A15}$$

Here, $L_{\rm peak}$ is measured at $(1+z)$ times the frequency that corresponds to the $F_{\rm lim}$. With $z < 0.1$, this so-called K-correction is a weak function of redshift and we therefore obtain a simple estimate of the volume out to which each TDE can be detected:

$$\mathcal{V}_j \propto D_{\rm max}^3 \propto \left(L_{g,{\rm peak},j}\right)^{3/2}. \tag{A16}$$

As the absolute value of the likelihood is not of interest to this calculation, one can define likelihood weights for each TDE with respect to (e.g.) a reference luminosity $L_0 = 10^{43}\,{\rm erg\,s^{-1}}$, or explicitly

$$w_j \propto \frac{1}{\mathcal{V}_j} = \left(\frac{L_{g,{\rm peak},j}}{L_0}\right)^{-3/2}. \tag{A17}$$

A2 Practical implementation of formalism

Given a set of starting distributions with tuneable parameters $\{\xi_i\}$, and an observational set $\{L_j\}$, the only non-trivial step actually required in computing the likelihood is performing the integral

$$p_L(l, \{\xi_i\}) \propto \iint\!\!\dots\!\int p_\Psi(\psi, \{\xi_i\})\, \delta\left(l - f(\psi)\right)\, {\rm d}^N\psi. \tag{A18}$$

For the problem at hand, we are interested in constraining parameters only in the black hole mass distribution. We are interested therefore in solving the integral

$$\begin{aligned} p_L(l, \{\xi_i\}) \propto & \int p_{M_\bullet}(m_\bullet, \{\xi_i\}) \int p_{A_\bullet}(a_\bullet) \int p_{M_\star}(m_\star) \\ & \times \int p_{\Theta_{\rm obs}}(\theta_{\rm obs}) \int p_{\Phi_{\rm orb}}(\phi_{\rm orb}) \dots \\ & \Theta\left(M_{\rm hills}(a_\bullet, m_\star, \phi_{\rm orb}, \dots) - m_\bullet\right) \delta\left(l - f(m_\bullet, a_\bullet, m_\star, \theta_{\rm obs}, \dots)\right) \\ & \times {\rm d}m_\bullet\, {\rm d}a_\bullet\, {\rm d}m_\star\, {\rm d}\theta_{\rm obs}\, {\rm d}\phi_{\rm orb} \dots, \end{aligned} \tag{A19}$$

Computing this integral is non-trivial for two main reasons: the coupling between parameters introduced by the Hills mass and the non-analytical nature of the plateau luminosity function f (the plateau luminosity for a given parameter set $\{\Psi\}$ is computed numerically). Even if we were to analytically write down an approximation for f, the Hills mass coupling still makes this integral non-trivial to compute analytically. We therefore turn to a numerical approach to approximating this integral.

Fortunately, both the Heaviside theta function (modelling the Hills mass) and the delta function act only as simple binary switches, and this integral is therefore easily approximated by Monte Carlo techniques. Formally, in the limit $N_{\rm sample} \to \infty$, the following procedure (written in pseudo-code) asymptotes exactly to p_L:

(i) Sample a set of parameters from each of the specified distributions $m_{\bullet,k} \sim p_{M_\bullet}(m_\bullet, \{\xi_i\})$, $m_{\star,k} \sim p_{M_\star}(m_\star)$, ...
(ii) Check if $M_{\rm hills}(a_{\bullet,k}, m_{\star,k}, \dots) > m_{\bullet,k}$.
(iii) If so, compute $l_k = f\left(m_{\bullet,k}, a_{\bullet,k}, m_{\star,k}, \theta_k, \dots\right)$.
(iv) Repeat $k = 1, 2, 3, \dots, N_{\rm sample}$ times.
(v) Construct a normalized histogram $\widetilde{p}_L(l, \{\xi_i\}; N_{\rm sample})$ of the $\{l_k\}$ luminosities.
(vi) In the limit $N_{\rm sample} \to \infty$, we have the following exact limit $\widetilde{p}_L(l, \{\xi_i\}; N_{\rm sample}) \to p_L(l, \{\xi_i\})$.
(vii) For large finite $N_{\rm sample}$, the function $\widetilde{p}_L(l, \{\xi_i\}; N_{\rm sample})$ will be a good approximation of the solutions to the required integrals.
(viii) One can then approximate $\log \widetilde{\mathcal{L}}\left(\{\xi_i\}\right) = \sum_{j=1}^{N_{\rm TDE}} \log \widetilde{p}_L\left(L_j, \{\xi_i\}; N_{\rm sample}\right)$, and perform standard techniques to fit for $\{\xi_\star\}$.

By experimenting numerically, we found that $N_{\rm sample} = 10^4$ was sufficient to remove noticeable stochasticity in $\widetilde{p}_L$. To avoid zero probability cases resulting from the finite $N_{\rm sample}$ used in this work, we smooth the luminosity histogram $\widetilde{p}_L$ by using Gaussian kernel density estimation.

APPENDIX B: TDE DISCOVERY REFERENCES

In Tables B1 and B2, we list the properties, and discovery references, of the new TDEs used in this work.

Table B1. The galactic properties of the 14 new TDEs in our sample. The quoted error ranges correspond to 1σ uncertainties.

TDE name	σ ($\mathrm{km\,s^{-1}}$)	$\log_{10} M_{\rm gal}$ ($\log_{10} \mathrm{M}_\odot$)
AT2017eqx	–	$9.43^{+0.08}_{-0.08}$
AT2018bsi	118^{+8}_{-8}	$10.64^{+0.06}_{-0.06}$
AT2019eve	–	$9.29^{+0.17}_{-0.17}$
AT2021ack	–	$10.13^{+0.02}_{-0.02}$
AT2021gje	–	$11.00^{+0.10}_{-0.10}$
AT2021lo	–	$10.08^{+0.14}_{-0.14}$
AT2022dbl	70^{+6}_{-6}	$10.04^{+0.06}_{-0.06}$
AT2022bdw	86^{+6}_{-5}	$10.04^{+0.03}_{-0.03}$
AT2022rz	–	$9.61^{+0.17}_{-0.17}$
AT2022dsb	–	$10.08^{+0.02}_{-0.02}$
AT2022hvp	–	$10.71^{+0.04}_{-0.04}$
AT2023clx	61^{+2}_{-2}	$9.94^{+0.11}_{-0.11}$
AT2020ksf	–	$9.91^{+0.09}_{-0.09}$
AT2020vdq	44^{+3}_{-3}	$9.04^{+0.16}_{-0.16}$

Table B2. The discovery papers for the additional TDEs used in this work.

TDE name	Reference
AT2017eqx	Nicholl et al. (2019)
AT2018bsi	van Velzen et al. (2021)
AT2019eve	van Velzen et al. (2021)
AT2020ksf	Wevers et al. (2024)
AT2020vdq	Somalwar et al. (2025)
AT2021ack	Hammerstein et al. (2021a)
AT2021gje	Hammerstein et al. (2021b)
AT2021lo	Yao et al. (2022)
AT2022dbl	Arcavi et al. (2022a)
AT2022bdw	Arcavi et al. (2022b)
AT2022rz	Hammerstein et al. (2022)
AT2022hvp	Fulton et al. (2022a)
AT2022dsb	Fulton et al. (2022b)
AT2023clx	Charalampopoulos et al. (2024)

This paper has been typeset from a TEX/LATEX file prepared by the author.